

Bending rigidity, sound propagation and ripples in flat graphene

Received: 7 June 2023

Accepted: 16 February 2024

Published online: 16 May 2024



Unai Aseginolaza^{1,2,3}, Josu Diego^{1,2}, Tommaso Cea^{4,5,6,7},
Raffaello Bianco^{1,8,9,10}, Lorenzo Monacelli¹¹, Francesco Libbi¹¹,
Matteo Calandra^{12,13}, Aitor Bergara^{1,14,15}, Francesco Mauri^{6,7} &
Ion Errea^{1,2,14} ✉

Many of the applications of graphene rely on its uneven stiffness and high thermal conductivity, but the mechanical properties of graphene—and, in general, of all two-dimensional materials—are still not fully understood. Harmonic theory predicts a quadratic dispersion for the out-of-plane flexural acoustic vibrational mode, which leads to the unphysical result that long-wavelength in-plane acoustic modes decay before vibrating for one period, preventing the propagation of sound. The robustness of quadratic dispersion has been questioned by arguing that the anharmonic phonon–phonon interaction linearizes it. However, this implies a divergent bending rigidity in the long-wavelength regime. Here we show that rotational invariance protects the quadratic flexural dispersion against phonon–phonon interactions, and consequently, the bending stiffness is non-divergent irrespective of the temperature. By including non-perturbative anharmonic effects in our calculations, we find that sound propagation coexists with a quadratic dispersion. We also show that the temperature dependence of the height fluctuations of the membrane, known as ripples, is fully determined by thermal or quantum fluctuations, but without the anharmonic suppression of their amplitude previously assumed. These conclusions should hold for all two-dimensional materials.

The theoretical comprehension of the mechanical properties of two-dimensional (2D) materials and membranes, which affect their acoustic and thermal properties, is one of the oldest problems in condensed-matter physics, dating back to the times in which the possibility of having 2D crystalline order was questioned^{1,2}. Even if the discovery of graphene and other 2D materials^{3–5} put aside this problem,

the understanding of how these materials can propagate sound and what their bending rigidity and ripple amplitude are is still under strong debate^{6–21}.

Most of the theoretical problems are caused by the quadratic dispersion of the acoustic flexural out-of-plane (ZA) mode that is obtained in the harmonic approximation. Such a quadratic dispersion

¹Centro de Física de Materiales CFM, CSIC-UPV/EHU, Donostia/San Sebastián, Spain. ²Fisika Aplikatua Saila, University of the Basque Country (UPV/EHU), Donostia/San Sebastián, Spain. ³Basic Sciences Department, Faculty of Engineering, Mondragon Unibertsitatea, Arrasate, Spain. ⁴Department of Physical and Chemical Sciences, Università degli Studi dell'Aquila, L'Aquila, Italy. ⁵Imdea Nanoscience, Madrid, Spain. ⁶Dipartimento di Fisica, Università di Roma La Sapienza, Rome, Italy. ⁷Graphene Labs, Fondazione Istituto Italiano di Tecnologia, Genoa, Italy. ⁸Ruder Bošković Institute, Zagreb, Croatia. ⁹Dipartimento di Scienze Fisiche, Informatiche e Matematiche, Università di Modena e Reggio Emilia, Modena, Italy. ¹⁰Centro S3, Istituto Nanoscienze-CNR, Modena, Italy. ¹¹Theory and Simulation of Materials (THEOS), École Polytechnique Fédérale de Lausanne, Lausanne, Switzerland. ¹²Dipartimento di Fisica, Università di Trento, Povo, Italy. ¹³Sorbonne Universités, CNRS, Institut des Nanosciences de Paris, Paris, France. ¹⁴Donostia International Physics Center (DIPC), Donostia/San Sebastián, Spain. ¹⁵Departamento de Física and EHU Quantum Center, University of the Basque Country (UPV/EHU), Bilbao, Spain. ✉e-mail: ion.errea@ehu.eus

also implies the unphysical result that graphene and other 2D membranes do not propagate sound. Indeed, the phonon linewidths of the in-plane acoustic longitudinal (LA) and transverse (TA) phonons calculated perturbatively from the harmonic result do not vanish in the long-wavelength limit^{22,23}, precisely because of the quadratic dispersion of the ZA modes²³. This yields the conclusion that phonons having sufficiently small momentum do not live long enough for vibrating one period, and thus, the quasiparticle picture is lost together with the propagation of sound²³.

It has been argued^{24–32} that the anharmonic coupling between in-plane and out-of-plane phonon modes renormalizes the dispersion of ZA phonons, providing it with a linear term at small momenta that somewhat cures the pathologies. It has long been assumed^{6,33} that the out-of-plane vibrational frequency of any continuous membrane acquires a linear term at small wavevectors once anharmonic interactions are included. The linear term stiffens the membrane and consequently suppresses the amplitude of its ripples, which is usually studied from the height correlation function in momentum space, namely, $\langle |h(\mathbf{q})|^2 \rangle$. In the classical harmonic approximation, it scales as $\langle |h(\mathbf{q})|^2 \rangle \propto q^{-4}$ and it is corrected to $q^{-4+\eta}$, with $\eta \approx 0.80–0.85$, when the ZA mode is linearized^{6,28–30,33}. Since the bending rigidity scales as $\kappa(\mathbf{q}) \propto 1/(\langle |h(\mathbf{q})|^2 \rangle q^4)$ in the classical limit⁶, this interpretation implies that the bending stiffness of all the membranes and 2D materials diverges in the long-wavelength limit, yielding the dubious interpretation that the larger the membrane, the stiffer it becomes. The experimental confirmation of these ideas is challenging due to the difficulties in measuring the bending rigidity of graphene^{34,35} and the substrate effects on the dispersion of ZA modes measured with helium diffraction^{36–39}.

The quadratic dispersion expected for the ZA mode in the harmonic approximation is imposed by the fact that the potential energy has to be invariant to a rotation of the system, irrespective of where the atoms sit. In the harmonic case, phonon frequencies are obtained by diagonalizing the $\phi_{ab}/\sqrt{M_a M_b}$ dynamical matrix, where a and b represent both atom and Cartesian indices, M_a is the mass of atom a and $\phi_{ab} = \left[\frac{\partial^2 V}{\partial R_a \partial R_b} \right]_0$ are the second-order force constants obtained as the second-order derivatives of the Born–Oppenheimer potential V with respect to atomic positions \mathbf{R} calculated at the positions that minimize V . Rotational invariance, together with the fact that in a strictly 2D system force constants involving an in-plane and out-of-plane displacement vanish, makes the ZA mode acquire a quadratic dispersion close to the zone centre²⁶. Phonons expected experimentally, however, should be calculated from the imaginary part of the phonon Green's function that includes anharmonic effects⁴⁰. For low-energy modes, such as the ZA mode, dynamical effects can be safely neglected. In this static limit, the phonon peaks coincide with the eigenvalues of the free energy Hessian $\left[\frac{\partial^2 F}{\partial \mathbf{R}_a \partial \mathbf{R}_b} \right]_0 / \sqrt{M_a M_b}$ for any theory in the static limit (Methods provides the proof), where F is the anharmonic free energy, \mathbf{R} is the average ionic position and the derivative is taken at the position that minimizes F (ref. 40). This raises a formidable remark that has remained unnoticed thus far: as both F and V are rotationally invariant, a quadratic dispersion should be expected for the ZA mode not only in the harmonic limit but also when anharmonic interactions are considered.

We dig into this point by accounting for anharmonicity beyond the perturbation theory within the self-consistent harmonic approximation (SCHA). The SCHA is applied in its stochastic implementation^{40–42} by making use of a machine-learning atomistic potential⁴³ as well as that with a membrane continuum Hamiltonian. The SCHA is a variational method that minimizes the free energy of the system

$$F = \langle T + V + \frac{1}{\beta} \ln \rho_{\mathbf{R}\Phi} \rangle_{\rho_{\mathbf{R}\Phi}} \quad (1)$$

with respect to a density matrix $\rho_{\mathbf{R}\Phi}$ parametrized with centroid positions \mathbf{R} and auxiliary force constants Φ (bold symbols represent vectors or tensors in compact notation). In equation (1), T is the ionic kinetic energy, β is the inverse temperature and $\langle O \rangle_{\rho_{\mathbf{R}\Phi}} = \text{Tr}[\rho_{\mathbf{R}\Phi} O]$ (O is any operator). We call auxiliary the phonon frequencies obtained by diagonalizing the $\phi_{ab}/\sqrt{M_a M_b}$ matrix. These frequencies include non-perturbative anharmonic corrections as they result from the variational minimization of F that fully includes V . However, phonons probed experimentally are related to the peaks in the imaginary part of the analytical continuation of the interacting Green's function $G_{ab}(\omega + i\delta)$ (refs. 40,44,45), which can be calculated from the

$$G_{ab}^{-1}(i\Omega_n) = G_{ab}^{-1(S)}(i\Omega_n) - \Pi_{ab}(i\Omega_n) \quad (2)$$

Dyson's equation, where Ω_n are bosonic Matsubara's frequencies. In equation (2), $G_{ab}^{-1(S)}(i\Omega_n) = (i\Omega_n)^2 \delta_{ab} - \phi_{ab}/\sqrt{M_a M_b}$ is the non-interacting Green's function formed by the auxiliary phonons and $\Pi(i\Omega_n)$ is the phonon–phonon interaction self-energy, which we estimate within the SCHA (Methods). The peaks in the imaginary part of $G_{ab}(\omega + i\delta)$ determine the frequencies and linewidths of the physical phonons. In the static $\omega = 0$ limit, the peaks coincide with the eigenvalues of the free energy Hessian. The frequencies derived from these peaks go beyond a mean-field picture, as they include many more interactions than the auxiliary ones⁴⁰, which would instead correspond to the mean-field solution.

To preserve rotational invariance, we make sure that the lattice parameter in our calculations sets the SCHA stress tensor⁴² to zero at each temperature. The lattice parameter thus calculated includes anharmonic effects as well as the effect of quantum and thermal fluctuations. All the phonon spectra shown in this work obtained with the atomistic potential are calculated with the lattice parameter that gives a null stress at each temperature. The harmonic spectra on the contrary are always calculated at the lattice parameter that minimizes V . The temperature dependence of the lattice parameter is shown in Fig. 1a. We include the molecular dynamics (MD) results from another work obtained with the same potential⁴³, which do not account for quantum effects. For comparison, we also include SCHA calculations in the classical limit, by making $\hbar = 0$ in $\rho_{\mathbf{R}\Phi}$, and within the quasi-harmonic (QH) approximation. Our quantum calculations correctly capture the negative thermal expansion of graphene that has been estimated in previous theoretical works^{27,43}. Our SCHA result shows a larger lattice parameter than the classical result. This is not surprising as classical calculations neglect quantum fluctuations and consequently underestimate the fluctuations associated with high-energy optical modes (the highest-energy phonon modes require temperatures of around 2,000 K to be thermally populated). This remarks the importance of considering quantum effects in the evaluation of the thermodynamic properties of graphene. Our classical results and the MD calculations⁴³ are in agreement at low temperatures.

In Fig. 1b–e, we compare the harmonic phonon spectra with the auxiliary phonons as well as with the spectra obtained from the peaks in the imaginary part of the inverse of the interacting Green's function—the physical phonons. The main conclusion is that although the mean-field dispersion of the ZA modes obtained from Φ is linearized, the physical phonons become close to a quadratic dispersion and approach the harmonic dispersion, as expected by rotational invariance in the static limit. This is very clear in Fig. 1d,e, where we show that the bending rigidity, defined as the frequency divided by the squared momentum, is independent of the wavevector at any temperature. This suggests that the bending rigidity is barely affected by interactions, in contradiction to the broadly assumed result that it diverges at small momentum in membranes due to thermal fluctuations⁶.

Even if the anharmonic correction to the phonon spectra may look small in Fig. 1, it has a huge impact on the acoustic properties of graphene. As shown in Fig. 2, the SCHA non-perturbative calculation

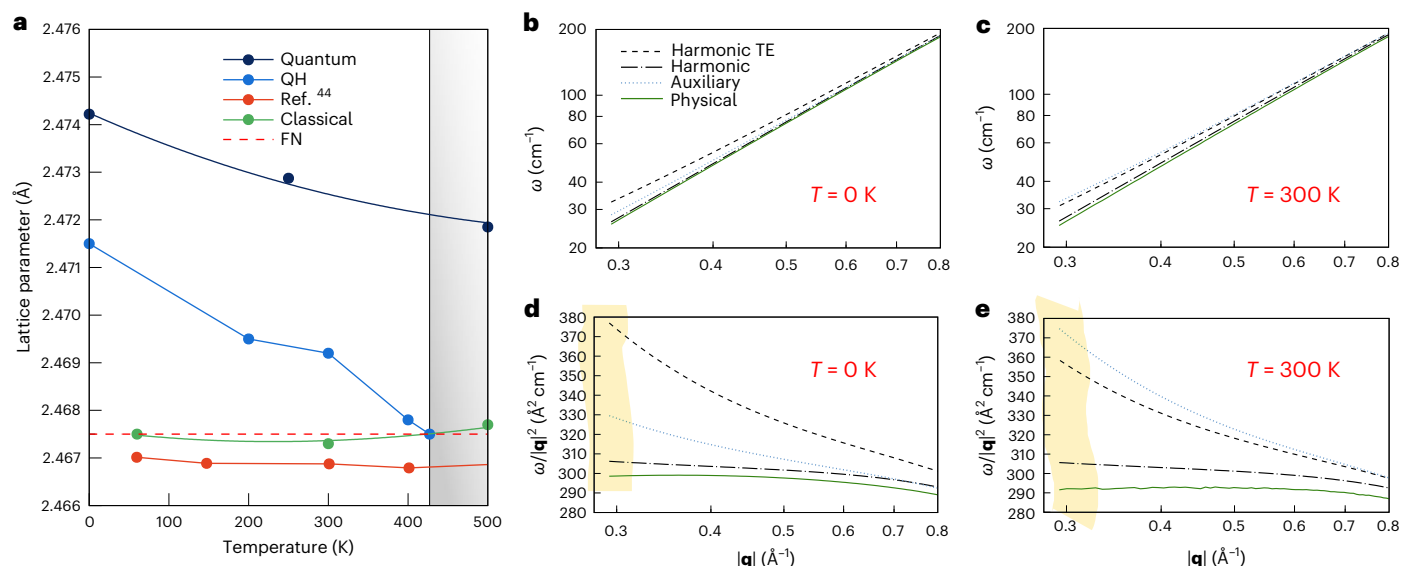


Fig. 1 | Mechanical properties of graphene calculated with the atomistic potential. **a**, Lattice parameter of graphene as a function of temperature obtained with the SCHa using a machine-learning atomistic potential. Both quantum and classical calculations are included. The temperature-independent frozen nuclei (FN) result corresponds to the lattice parameter that minimizes the Born–Oppenheimer potential V . The MD results from another work⁴³ are included. The lattice parameter calculated in the QH approximation is also included. In the grey zone, harmonic phonons become unstable, breaking down the QH approximation. **b–e**, Harmonic ZA phonon spectra together with the

SCHa auxiliary phonons and the physical phonons obtained from the peaks of Green's function in equation (2) at 0 K (**b**) and 300 K (**c**). Panels **d** and **e** show the bending rigidity, defined as the frequency divided by the squared momentum. In these panels, the dispersion corresponds to the Γ –M direction. For reference, the M point is at 1.4662 \AA^{-1} at 0 K and at 1.4671 \AA^{-1} at 300 K. The harmonic result (solid black) is computed at the lattice parameter that minimizes V , whereas the other results include thermal expansion (TE). The dashed black lines correspond to harmonic calculations including thermal expansion (TE).

based on equation (2) dramatically changes the linewidth of the LA and TA modes at small momenta by making them smaller as momentum decreases, in clear contrast to the perturbative calculation obtained on top of the harmonic result. This happens because of the linearization of auxiliary flexural phonons that form the non-interacting Green's function and enter in Dyson's equation. When the ratio between the full-width at half-maximum (FWHM) and the frequency of the mode is approximately 1, the quasiparticle picture is lost. This value is reached in the momentum range of 0.001 – 0.002 \AA^{-1} in the harmonic case. However, when the linewidth is calculated within the SCHa, the ratio never gets bigger than 0.05. These results recover the quasiparticle picture for in-plane acoustic modes at any wavevector, guaranteeing that graphene always propagates sound. The momentum range for which the quasiparticle picture is lost in harmonic approximation can be experimentally reached with Brillouin scattering probes. In fact, for few-layer graphene, the quasiparticle picture holds in the 0.001 – 0.002 \AA^{-1} region⁴⁶, in agreement with our calculations. We show here that there is no need of strain²³ to have physically well-defined phonon linewidths in graphene.

To obtain results at very small momenta and reinforce the conclusions drawn with the atomistic calculations, we solve the SCHa equations in a continuum membrane Hamiltonian. This model has been widely used in the literature to describe graphene as an elastic membrane as well as to account for the coupling between in-plane and out-of-plane acoustic modes^{6,28–30,33}. The most general rotationally invariant continuum potential to describe a free-standing 2D membrane up to the fourth order in the phonon fields has the following form⁴⁷:

$$V = \frac{1}{2} \int_{\Omega} d^2x \left(\kappa (\partial^2 h)^2 + C^{ijkl} u_{ij} u_{kl} \right), \quad (3)$$

$$u_{ij} = \frac{1}{2} (\partial_i u_j + \partial_j u_i + \partial_i \mathbf{u} \cdot \partial_j \mathbf{u} + \partial_i h \partial_j h). \quad (4)$$

Here $\mathbf{u}(\mathbf{x})$ and $h(\mathbf{x})$ are the in-plane and out-of-plane displacement fields, respectively; u_{ij} is the stress tensor; and \mathbf{x} is the 2D position vector in the membrane. Also, κ is the harmonic bending rigidity of the membrane, Ω is the area of the membrane and the tensor $C^{ijkl} = \lambda \delta^{ij} \delta^{kl} + \mu (\delta^{ik} \delta^{jl} + \delta^{il} \delta^{jk})$ contains the Lamé coefficients λ and μ . We have calculated the parameters by fitting them to the atomistic potential, which yields $\lambda = 4.3 \text{ eV \AA}^{-2}$, $\mu = 9.3 \text{ eV \AA}^{-2}$, $\kappa = 1.5 \text{ eV}$ and $\rho/\hbar^2 = 1,097 \text{ eV}^{-1} \text{ \AA}^{-4}$. This continuum model only accounts for acoustic modes. The harmonic acoustic frequencies given by equation (3) are $\omega_{ZA}(q) = \sqrt{\kappa/\rho} q^2$, $\omega_{LA}(q) = \sqrt{(\lambda + 2\mu)/\rho} q$ and $\omega_{TA}(q) = \sqrt{\mu/\rho} q$, where ρ is the mass density of the membrane. The thermal expansion is included in this formalism by changing the in-plane derivatives as $\partial_i u_j \rightarrow \partial_i u_j + \delta^{ij} \delta a$, where $\delta a = (a - a_0)/a_0$ and a_0 is the lattice parameter that minimizes V .

The results obtained in this rotationally invariant membrane are shown in Fig. 3. All the conclusions drawn with the atomistic model are confirmed and put in solid grounds. Again, the mean-field ZA phonons obtained from the auxiliary SCHa force constants get linearized at small momenta. However, when the interacting physical phonons are calculated from the free energy Hessian (due to the low frequencies of the ZA modes, this static approximation is perfectly valid (Extended Data Fig. 1)), the ZA phonon frequencies get on top of the harmonic values, recovering a quadratic dispersion. This means that the physical phonons have a quadratic dispersion for small momenta in an unstrained membrane, as it is expected by rotational invariance, and that the bending rigidity does not increase in the long-wavelength limit and is barely affected by interactions. Consequently, the bending rigidity that we obtain is around the harmonic value of 1.5 eV, in good agreement with the experimental results from other works^{37,39}. Figure 3 remarks that correctly accounting for thermal expansion is crucial to recover the quadratic dispersion of flexural modes. The validity of the membrane potential is confirmed by calculating the linewidths of the LA and TA modes, which yield consistent results to those obtained with the atomistic potential (Fig. 2).

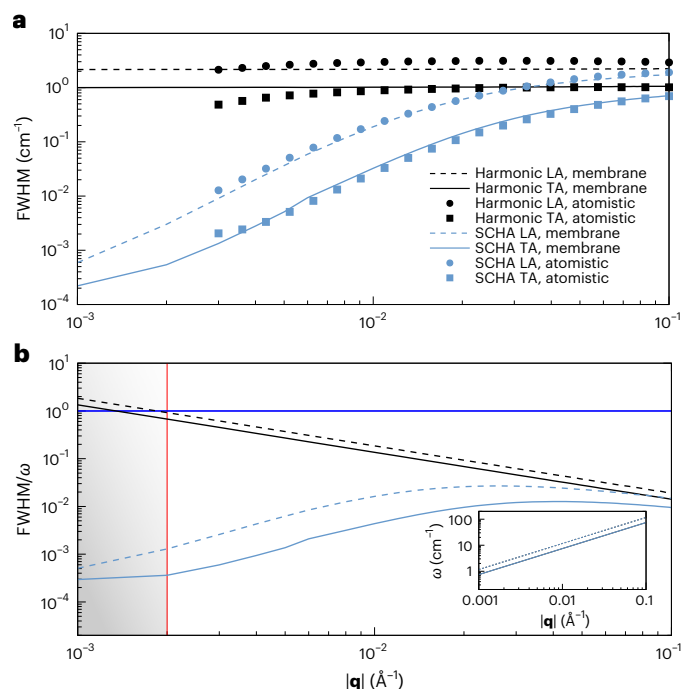


Fig. 2 | Sound propagation in graphene. **a**, Linewidths (FWHM) of LA and TA phonon modes at 300 K calculated within the perturbation theory on top of the harmonic result and within the SCHA following equation (2). The squares and circles are calculated with the atomistic potential and lines correspond to calculations within the membrane model. Our harmonic results are in good agreement with other theoretical calculations^{22,23}. **b**, FWHM divided by the phonon frequency in the membrane model. In the inset, we show the phonon frequencies in the same momentum range. The grey zone corresponds to the region where the fraction FWHM_{LA}/ω_{LA} is bigger than one in the harmonic case.

Our results, thus, upturn the conventional wisdom of 2D membranes^{6,28–30,33}: interactions do not linearize the dispersion of ZA mode and the bending rigidity does not diverge at small momentum. The main reason for this is that in previous works, the $\partial_{\mathbf{u}} \cdot \partial_{\mathbf{u}}$ term in the stress tensor, which guarantees the rotational invariance of the potential (Methods), is neglected, unavoidably lowering the power of the ZA phonon frequency to $\Omega_{\text{ZA}}(\mathbf{q}) \propto q^d$ (Fig. 3a), where $d \approx 1.6$ in our case in the range of wavenumbers studied, even if in the ultimate $q \rightarrow 0$ limit, we expect a linear dispersion in our quantum calculation (Methods), as suggested elsewhere²⁹. The amplitude of the height fluctuations or ripples in the long-wavelength limit reflects the absence of rotational invariance in prior calculations. Different calculations within the self-consistent screening approximation (SCSA) or non-perturbative renormalization group theory yield consistent values of $\langle |h(\mathbf{q})|^2 \rangle \propto q^{-4+\eta}$, where $\eta \approx 0.80$ – 0.85 (refs. 6,28–30,33,48,49). We can estimate $\langle |h(\mathbf{q})|^2 \rangle$ within the SCHA in our membrane model by calculating the equal-time out-of-plane displacement correlation function, which—in the static limit—leads to the following simple equation (Methods):

$$\langle |h(\mathbf{q})|^2 \rangle = \frac{(1 + 2n_B(\Omega_{\text{ZA}}(\mathbf{q})))}{2\rho\Omega_{\text{ZA}}(\mathbf{q})}, \quad (5)$$

where $n_B(\omega)$ is the bosonic occupation factor and $\Omega_{\text{ZA}}(\mathbf{q})$ is the interacting physical flexural phonon frequency coming from the free energy Hessian. The presence of bosonic occupation completely determines the dependence on \mathbf{q} of the correlation function: in the classical limit, when the temperature is larger than the frequency of the ZA mode, $\langle |h(\mathbf{q})|^2 \rangle \propto \Omega_{\text{ZA}}(\mathbf{q})^{-2}$, whereas in the quantum limit, when the ZA mode is unoccupied, $\langle |h(\mathbf{q})|^2 \rangle \propto \Omega_{\text{ZA}}(\mathbf{q})^{-1}$. In the classical regime, we recover the $\langle |h(\mathbf{q})|^2 \rangle \propto q^{-3.2}$ behaviour when we neglect $\partial_{\mathbf{u}} \cdot \partial_{\mathbf{u}}$ (Fig. 4), showing

that our result is consistent with previous calculations within SCSA and non-perturbative renormalization group methods in the wavenumber range studied^{6,28–30,33,48,49}. However, when we keep full rotational invariance, the ZA modes acquire a quadratic dispersion and thus $\langle |h(\mathbf{q})|^2 \rangle \propto q^{-4}$, which is the result obtained in the harmonic case. Consequently, anharmonicity does not suppress the amplitude of ripples in the long-wavelength limit, upturning the previous consensus^{6,28–30,33}. It should be stressed that correctly accounting for thermal expansion and not using a fixed lattice parameter a_0 is crucial to recover the quadratic dispersion of the ZA mode (Fig. 3) as well as the consequent q^{-4} power law of the height correlation function. This explains why the renormalization group calculations presented in another work⁵⁰ did not recover a q^{-4} behaviour even when the Hamiltonian contained the $\partial_{\mathbf{u}} \cdot \partial_{\mathbf{u}}$ term and was, thus, rotationally invariant.

The crossover between the regimes in which thermal and quantum fluctuations determine the ripples (Fig. 4) is in very good agreement with the conclusions drawn with atomistic path-integral Monte Carlo simulations of free-standing graphene⁵¹. This crossover occurs at different wavenumbers depending on the temperature, basically when $\hbar\Omega_{\text{ZA}}(\mathbf{q}) \approx k_B T$. However, atomistic classical Monte Carlo and MD simulations have estimated $\langle |h(\mathbf{q})|^2 \rangle$ for small wavenumbers in the order of $q \approx 0.01$ Å⁻¹, finding a scaling law not far from the $q^{-3.2}$ one obtained in the membrane model when rotational invariance is broken^{725,49,51,52}. Even if this contradicts our results since such atomistic calculations, in principle, respect rotational invariance, an uncontrollable strain in the numerical simulations as small as $\delta a = 10^{-5}$ is enough to lower the exponent from -4.0 to -3.2 in the long-wavelength limit (Extended Data Fig. 2). Considering that the ZA mode with $q \approx 0.01$ Å⁻¹ requires about 1 ns to perform one period, very long simulation times are required to describe a thermodynamically flat phase of graphene, and thus, these Monte Carlo and MD numerical simulations may also be affected by

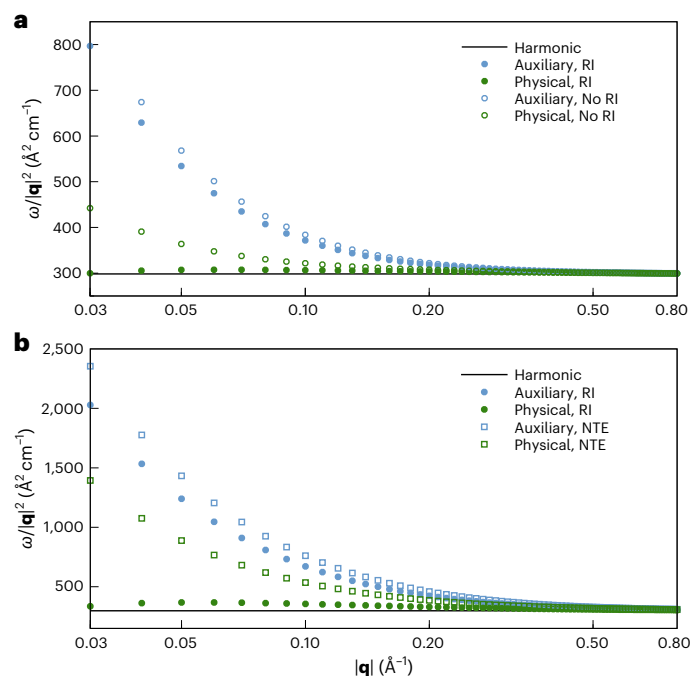


Fig. 3 | Bending rigidity of graphene in the membrane model. **a**, Bending rigidity of graphene, defined as the ratio between the frequency of the ZA mode divided by the squared momentum, calculated within the harmonic approximation and within the SCHA auxiliary and physical cases at 0 K in the membrane model. Results considering the full potential in equation (3) are termed rotationally invariant (RI). Results neglecting the $\partial_{\mathbf{u}} \cdot \partial_{\mathbf{u}}$ term in equation (4) are termed not rotationally invariant (No RI). **b**, Same results as in **a** but at 300 K with the full membrane potential in the rotationally invariant case. We also include the results without considering thermal expansion (NTE).

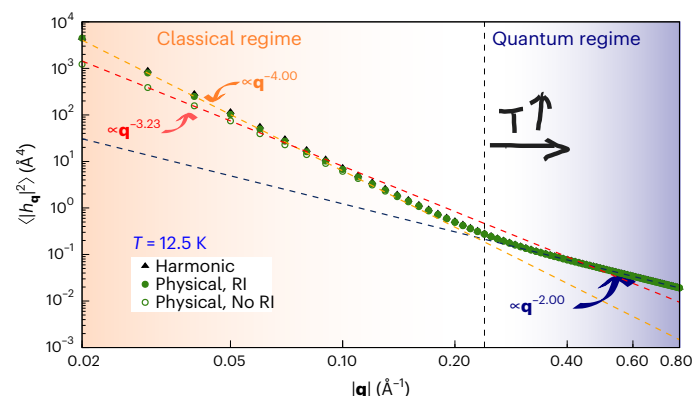


Fig. 4 | Fourier transform of the height–height correlation function in the membrane model. Fourier transform of the height–height correlation function at 12.5 K in the membrane model evaluated at different levels of approximation: harmonic (black dots), anharmonic RI result (green filled dots) and anharmonic No RI result (green empty dots). The dashed vertical line specifies the wavevector at which the crossover from classical (orange background) to quantum (violet background) correlations occurs at this temperature. The dashed lines correspond to linear fits with different exponents.

High T favours ergodic?

non-ergodic conditions, affecting the determination of the height correlation function in the long-wavelength limit. On the contrary, in our SCHA simulations, the centroids are always in the plane. Our results indeed show that this flat configuration is a minimum of the free energy at the studied temperatures.

The conclusions presented here are universal and can be extrapolated to any strictly 2D material or membrane, offering a new perspective in the understanding of their thermodynamic, mechanical and vibrational properties. Even if complex hydrodynamic behaviour dominates the thermal conductivity of 2D materials⁵³, the effects on the dispersion and lifetimes of acoustic modes found here may be relevant for the calculation of the thermal conductivity of 2D crystals. Our results open new doors for calculating all of these properties.

Online content

Any methods, additional references, Nature Portfolio reporting summaries, source data, extended data, supplementary information, acknowledgements, peer review information; details of author contributions and competing interests; and statements of data and code availability are available at <https://doi.org/10.1038/s41567-024-02441-z>.

References

- Landau, L. D. & Lifshitz, E. M. *Statistical Physics* (Pergamon, 1980).
- Mermin, N. D. Crystalline order in two dimensions. *Phys. Rev.* **176**, 250 (1968).
- Novoselov, K. S. et al. Electric field effect in atomically thin carbon films. *Science* **306**, 666–669 (2004).
- Novoselov, K. S. et al. Two-dimensional atomic crystals. *Proc. Natl Acad. Sci. USA* **102**, 10451–10453 (2005).
- Meyer, J. C. et al. The structure of suspended graphene sheets. *Nature* **446**, 60–63 (2007).
- Nelson, D. R. & Peliti, L. Fluctuations in membranes with crystalline and hexatic order. *J. Phys. France* **48**, 1085–1092 (1987).
- Fasolino, A., Los, J. H. & Katsnelson, M. I. Intrinsic ripples in graphene. *Nat. Mater.* **6**, 858–861 (2007).
- Gazit, D. Correlation between charge inhomogeneities and structure in graphene and other electronic crystalline membranes. *Phys. Rev. B* **80**, 161406 (2009).
- Gazit, D. Structure of physical crystalline membranes within the self-consistent screening approximation. *Phys. Rev. E* **80**, 041117 (2009).
- San-Jose, P., González, J. & Guinea, F. Electron-induced rippling in graphene. *Phys. Rev. Lett.* **106**, 045502 (2011).
- Bonilla, L. L. & Carpio, A. Ripples in a graphene membrane coupled to Glauber spins. *J. Stat. Mech.* **2012**, P09015 (2012).
- Guinea, F., Le Doussal, P. & Wiese, K. J. Collective excitations in a large- d model for graphene. *Phys. Rev. B* **89**, 125428 (2014).
- González, J. Rippling transition from electron-induced condensation of curvature field in graphene. *Phys. Rev. B* **90**, 165402 (2014).
- Ruiz-García, M., Bonilla, L. & Prados, A. Ripples in hexagonal lattices of atoms coupled to Glauber spins. *J. Stat. Mech.* **2015**, P05015 (2015).
- Gornyi, I. V., Kachorovskii, V. Y. & Mirlin, A. D. Rippling and crumpling in disordered free-standing graphene. *Phys. Rev. B* **92**, 155428 (2015).
- Ruiz-García, M., Bonilla, L. L. & Prados, A. STM-driven transition from rippled to buckled graphene in a spin-membrane model. *Phys. Rev. B* **94**, 205404 (2016).
- Bonilla, L. L. & Ruiz-García, M. Critical radius and temperature for buckling in graphene. *Phys. Rev. B* **93**, 115407 (2016).
- Gornyi, I. V., Dmitriev, A. P., Mirlin, A. D. & Protopopov, I. V. Electron in the field of flexural vibrations of a membrane: quantum time, magnetic oscillations, and coherence breaking. *J. Exp. Theor. Phys.* **123**, 322–347 (2016).
- Ruiz-García, M., Bonilla, L. L. & Prados, A. Bifurcation analysis and phase diagram of a spin-string model with buckled states. *Phys. Rev. E* **96**, 062147 (2017).
- Cea, T., Ruiz-García, M., Bonilla, L. & Guinea, F. Numerical study of the rippling instability driven by electron-phonon coupling in graphene. *Phys. Rev. B* **101**, 235428 (2020).
- Silva-Guillén, J. A. & Guinea, F. Electron heating and mechanical properties of graphene. *Phys. Rev. B* **101**, 060102 (2020).
- Paulatto, L., Mauri, F. & Lazzeri, M. Anharmonic properties from a generalized third-order ab initio approach: theory and applications to graphite and graphene. *Phys. Rev. B* **87**, 214303 (2013).
- Bonini, N., Garg, J. & Marzari, N. Acoustic phonon lifetimes and thermal transport in free-standing and strained graphene. *Nano Lett.* **12**, 2673–2678 (2012).
- Wang, H. & Daw, M. S. Anharmonic renormalization of the dispersion of flexural modes in graphene using atomistic calculations. *Phys. Rev. B* **94**, 155434 (2016).
- Los, J. H., Katsnelson, M. I., Yazyev, O. V., Zakharchenko, K. V. & Fasolino, A. Scaling properties of flexible membranes from atomistic simulations: application to graphene. *Phys. Rev. B* **80**, 121405 (2009).
- Katsnelson, M. I. & Fasolino, A. Graphene as a prototype crystalline membrane. *Acc. Chem. Res.* **46**, 97–105 (2013).
- Zakharchenko, K. V., Katsnelson, M. I. & Fasolino, A. Finite temperature lattice properties of graphene beyond the quasiharmonic approximation. *Phys. Rev. Lett.* **102**, 046808 (2009).
- Mariani, E. & Von Oppen, F. Flexural phonons in free-standing graphene. *Phys. Rev. Lett.* **100**, 076801 (2008).
- Amorim, B. et al. Thermodynamics of quantum crystalline membranes. *Phys. Rev. B* **89**, 224307 (2014).
- De Andres, P. L., Guinea, F. & Katsnelson, M. I. Bending modes, anharmonic effects, and thermal expansion coefficient in single-layer and multilayer graphene. *Phys. Rev. B* **86**, 144103 (2012).
- Michel, K. H., Costamagna, S. & Peeters, F. M. Theory of anharmonic phonons in two-dimensional crystals. *Phys. Rev. B* **91**, 134302 (2015).
- Michel, K. H., Scuracchio, P. & Peeters, F. M. Sound waves and flexural mode dynamics in two-dimensional crystals. *Phys. Rev. B* **96**, 094302 (2017).

33. Le Doussal, P. & Radzihovsky, L. Self-consistent theory of polymerized membranes. *Phys. Rev. Lett.* **69**, 1209–1212 (1992).
34. Blees, M. K. et al. Graphene kirigami. *Nature* **524**, 204–207 (2015).
35. Lindahl, N. et al. Determination of the bending rigidity of graphene via electrostatic actuation of buckled membranes. *Nano Lett.* **12**, 3526–3531 (2012).
36. Al Taleb, A., Anemone, G., Fariás, D. & Miranda, R. Acoustic surface phonons of graphene on Ni (111). *Carbon* **99**, 416–422 (2016).
37. Al Taleb, A., Yu, H.K., Anemone, G., Fariás, D. & Wodtke, A. M. Helium diffraction and acoustic phonons of graphene grown on copper foil. *Carbon* **95**, 731–737 (2015).
38. Al Taleb, A., Anemone, G., Fariás, D. & Miranda, R. Resolving localized phonon modes on graphene/Ir (111) by inelastic atom scattering. *Carbon* **133**, 31–38 (2018).
39. Tømterud, M. et al. Temperature dependent bending rigidity of graphene. Preprint at <https://doi.org/10.48550/arXiv.2210.17250> (2022).
40. Bianco, R., Errea, I., Paulatto, L., Calandra, M. & Mauri, F. Second-order structural phase transitions, free energy curvature, and temperature-dependent anharmonic phonons in the self-consistent harmonic approximation: theory and stochastic implementation. *Phys. Rev. B* **96**, 014111 (2017).
41. Errea, I., Calandra, M. & Mauri, F. Anharmonic free energies and phonon dispersions from the stochastic self-consistent harmonic approximation: application to platinum and palladium hydrides. *Phys. Rev. B* **89**, 064302 (2014).
42. Monacelli, L., Errea, I., Calandra, M. & Mauri, F. Pressure and stress tensor of complex anharmonic crystals within the stochastic self-consistent harmonic approximation. *Phys. Rev. B* **98**, 024106 (2018).
43. Rowe, P., Csányi, G., Alfè, D. & Michaelides, A. Development of a machine learning potential for graphene. *Phys. Rev. B* **97**, 054303 (2018).
44. Monacelli, L. & Mauri, F. Time-dependent self-consistent harmonic approximation: anharmonic nuclear quantum dynamics and time correlation functions. *Phys. Rev. B* **103**, 104305 (2021).
45. Lihm, J.-M. & Park, C.-H. Gaussian time-dependent variational principle for the finite-temperature anharmonic lattice dynamics. *Phys. Rev. Res.* **3**, L032017 (2021).
46. Wang, Z. K., Lim, H. S., Ng, S. C., Özyilmaz, B. & Kuok, M. H. Brillouin scattering study of low-frequency bulk acoustic phonons in multilayer graphene. *Carbon* **46**, 2133–2136 (2008).
47. Landau, L. D. & Lifshits, E. M. *Theory of Elasticity* (Addison-Wesley, 1959).
48. Kownacki, J.-P. & Mouhanna, D. Crumpling transition and flat phase of polymerized phantom membranes. *Phys. Rev. E* **79**, 040101 (2009).
49. Roldán, R., Fasolino, A., Zakharchenko, K. V. & Katsnelson, M. I. Suppression of anharmonicities in crystalline membranes by external strain. *Phys. Rev. B* **83**, 174104 (2011).
50. Coquand, O. & Mouhanna, D. Flat phase of quantum polymerized membranes. *Phys. Rev. E* **94**, 032125 (2016).
51. Hašik, J., Tosatti, E. & Martoňák, R. Quantum and classical ripples in graphene. *Phys. Rev. B* **97**, 140301 (2018).
52. Wei, D. & Wang, F. Graphene: a partially ordered non-periodic solid. *J. Chem. Phys.* **141**, 144701 (2014).
53. Cepellotti, A. et al. Phonon hydrodynamics in two-dimensional materials. *Nat. Commun.* **6**, 6400 (2015).

Publisher's note Springer Nature remains neutral with regard to jurisdictional claims in published maps and institutional affiliations.

Springer Nature or its licensor (e.g. a society or other partner) holds exclusive rights to this article under a publishing agreement with the author(s) or other rightsholder(s); author self-archiving of the accepted manuscript version of this article is solely governed by the terms of such publishing agreement and applicable law.

© The Author(s), under exclusive licence to Springer Nature Limited 2024

Methods

Anharmonic theory: SCHA

We study the lattice dynamics of graphene in the Born–Oppenheimer approximation; thus, we consider the quantum Hamiltonian for the atoms defined by the Born–Oppenheimer potential energy $V(\mathbf{R})$. Here \mathbf{R} is used to denote the component-free notation of $R^{\alpha s}(\mathbf{l})$, which is a collective coordinate that completely specifies the atomic configuration of the crystal. The index α denotes the Cartesian direction, s labels the atom within the unit cell and \mathbf{l} indicates the three-dimensional lattice vector. Hereafter, we will also use a single compact index $a = (\alpha, s, \mathbf{l})$ to indicate the Cartesian index α , atom index s and lattice vector \mathbf{l} . Moreover, in general, we will use bold letters to indicate other quantities in the component-free notation.

To take into account quantum effects and anharmonicity at a non-perturbative level, we use SCHA^{40–42}. For a given temperature T , the method allows to find an approximation for $F(\mathcal{R})$, the free energy of the crystal as a function of the average atomic positions \mathcal{R}^a (the centroids). For a given centroid \mathcal{R} , the SCHA free energy is obtained through an auxiliary quadratic Hamiltonian, namely, the SCHA Hamiltonian $\mathcal{H}_{\mathcal{R}\Phi}$, by variationally minimizing the free energy with respect to the SCHA centroids and auxiliary force constants Φ . The free energy Hessian, or the physical phonons in the static approach, can be computed by using the analytic formula (in the component-free notation) as

$$\frac{\partial^2 F}{\partial \mathcal{R} \partial \mathcal{R}} = \Phi + \Phi \Lambda(0) [\mathbf{1} - \Phi \Lambda(0)]^{-1} \Phi, \quad (6)$$

where

$$\Phi = \left\langle \frac{\partial^3 V}{\partial \mathbf{R} \partial \mathbf{R} \partial \mathbf{R}} \right\rangle_{\rho_{\mathcal{R}\Phi}}, \quad \Lambda = \left\langle \frac{\partial^4 V}{\partial \mathbf{R} \partial \mathbf{R} \partial \mathbf{R} \partial \mathbf{R}} \right\rangle_{\rho_{\mathcal{R}\Phi}} \quad (7)$$

and the averages are with respect to the density matrix of the SCHA Hamiltonian $\mathcal{H}_{\mathcal{R}\Phi}$, that is, $\rho_{\mathcal{R}\Phi} = e^{-\beta \mathcal{H}_{\mathcal{R}\Phi}} / \text{tr}[e^{-\beta \mathcal{H}_{\mathcal{R}\Phi}}]$ and $\beta = (k_B T)^{-1}$, where k_B is the Boltzmann constant. In equation (6), the value $z = 0$ of the fourth-order tensor $\Lambda(z)$ is used. For a generic complex number z , it is defined, in components, as

$$\Lambda^{abcd}(z) = -\frac{1}{2} \sum_{\mu\nu} \tilde{F}(z, \omega_\mu, \omega_\nu) \times \sqrt{\frac{\hbar}{2M_a\omega_\mu}} e_\mu^a \sqrt{\frac{\hbar}{2M_b\omega_\nu}} e_\nu^b \sqrt{\frac{\hbar}{2M_c\omega_\mu}} e_\mu^c \sqrt{\frac{\hbar}{2M_d\omega_\nu}} e_\nu^d, \quad (8)$$

where M_a is the mass of the atom a , ω_μ^2 (auxiliary phonons) are the eigenvalues and e_μ^a are the eigenvectors of $D_{ab}^{(S)} = \Phi_{ab}/\sqrt{M_a M_b}$; furthermore,

$$\tilde{F}(z, \omega_\mu, \omega_\nu) = \frac{2}{\hbar} \left[\frac{(\omega_\mu + \omega_\nu)[1 + n_B(\omega_\mu) + n_B(\omega_\nu)]}{(\omega_\mu + \omega_\nu)^2 - z^2} - \frac{(\omega_\mu - \omega_\nu)[n_B(\omega_\mu) - n_B(\omega_\nu)]}{(\omega_\mu - \omega_\nu)^2 - z^2} \right], \quad (9)$$

where $n_B(\omega) = 1/(e^{\beta\hbar\omega} - 1)$ is the bosonic occupation number.

As shown in other works^{40,44,45}, in the SCHA, the Green's function $\mathbf{G}(i\Omega_n)$ for the correlation of variable $\sqrt{M_a}(\mathcal{R}^a - \mathcal{R}^a)$ in the frequency domain (Ω_n is a Matsubara frequency) is given as

$$\mathbf{G}^{-1}(i\Omega_n) = (i\Omega_n)^2 \mathbf{1} - \mathbf{M}^{-\frac{1}{2}} \Phi \mathbf{M}^{-\frac{1}{2}} - \Pi(i\Omega_n), \quad (10)$$

where $\mathbf{G}^{-1}(0) = -\mathbf{D}^{(F)}$, $D_{ab}^{(F)} = \frac{1}{\sqrt{M_a M_b}} \frac{\partial^2 F}{\partial \mathcal{R}_a \partial \mathcal{R}_b}$ and $\Pi(z)$ is the SCHA self-energy, which is given by

$$\Pi(i\Omega_n) = \mathbf{M}^{-\frac{1}{2}} \Phi \Lambda(i\Omega_n) [\mathbf{1} - \Phi \Lambda(i\Omega_n)]^{-1} \Phi \mathbf{M}^{-\frac{1}{2}}. \quad (11)$$

Here $M_{ab} = \delta_{ab} M_a$ is the mass matrix. For the applications considered in the present paper, the static term $\Phi \Lambda(0)$ is negligible with respect to the identity matrix (Extended Data Fig. 3). Extending this approximation to the dynamical case reduces the SCHA self-energy to the so-called bubble self-energy, namely,

$$\Pi \approx \Pi^{(B)}(i\Omega_n) = \mathbf{M}^{-\frac{1}{2}} \Phi \Lambda(i\Omega_n) \Phi \mathbf{M}^{-\frac{1}{2}}. \quad (12)$$

We then neglect the mixing between different phonon modes and assume that $\Pi(i\Omega_n)$ is diagonal in the basis of the eigenvectors $e_\mu^a(\mathbf{q})$ of $\Phi_{ab}(\mathbf{q})/\sqrt{M_a M_b}$, where $\Phi_{ab}(\mathbf{q})$ is the Fourier transform of the real-space Φ (now a and b represent atoms in the unit cell and Cartesian indices). We then define

$$\Pi_\mu(\mathbf{q}, i\Omega_n) = \sum_{a,b} e_\mu^a(-\mathbf{q}) \Pi_{ab}(\mathbf{q}, i\Omega_n) e_\mu^b(\mathbf{q}). \quad (13)$$

In studying the response of a lattice to inelastic scattering experiments, we need the one-phonon spectral function. By using equation (10) for $\mathbf{G}(i\Omega_n)$, we can calculate the cross-section $\sigma(\omega) = -\omega \text{Tr} \text{Im} \mathbf{G}(\omega + i0^+)/\pi$, whose peaks signal the presence of collective vibrational excitations (physical phonons in the dynamic approach) having certain energies. Again, we take advantage of the lattice periodicity and we Fourier transform the interesting quantities with respect to the lattice indices. In particular, we consider the Fourier transform of the SCHA self-energy, namely, $\Pi_{ab}(\mathbf{q}, i\Omega_n)$. Neglecting the mixing between different modes, the cross-section is then given by

$$\sigma(\mathbf{q}, \omega) = \frac{1}{\pi} \sum_\mu \frac{-\omega \text{Im} \Pi_\mu(\mathbf{q}, \omega)}{(\omega^2 - \omega_\mu^2(\mathbf{q}) - \text{Re} \Pi_\mu(\mathbf{q}, \omega))^2 + (\text{Im} \Pi_\mu(\mathbf{q}, \omega))^2}. \quad (14)$$

If we neglect the frequency dependence of the phonon self-energy, we get the weakly anharmonic limit of the cross-section, which is going to be a sum of Lorentzian functions. These Lorentzians are well-defined physical phonons in the dynamical approach. The square of the phonon frequencies, $\Theta_\mu^2(\mathbf{q})$, corrected by the bubble self-energy is expressed as

$$\Theta_\mu^2(\mathbf{q}) = \omega_\mu^2(\mathbf{q}) + \text{Re} \Pi_\mu(\mathbf{q}, \omega_\mu(\mathbf{q})), \quad (15)$$

where $\omega_\mu^2(\mathbf{q})$ are the eigenvalues of the Fourier transform of $\mathbf{D}^{(S)}$. The linewidth of the phonons in equation (15) is proportional to $\text{Im} \Pi_\mu(\mathbf{q}, \omega_\mu(\mathbf{q}))$. The centres of these peaks are the ones supposed to be measured in inelastic experiments. By calculating $\Omega_\mu^2(\mathbf{q}) = \omega_\mu^2(\mathbf{q}) + \text{Re} \Pi_\mu(\mathbf{q}, 0)$, the static limit in equation (6) is recovered, namely, the eigenvalues of the free energy Hessian. Extended Data Fig. 1 shows that the dynamic effects are negligible in the ZA modes, meaning that the static approximation and phonons coming from the free energy Hessian are a good approximation for physical phonons.

Hessian of free energy and physical phonons in an exact theory

Here we provide proof that the physical phonons coincide with the eigenvalues of the free energy Hessian in an exact static theory as well at zero temperature, and that this is not a particular result of the SCHA. At 0 K, this is true if⁴⁰

$$-\frac{1}{\sqrt{M_a M_b}} \frac{\partial^2 E}{\partial \mathcal{R}_a \partial \mathcal{R}_b} = G_{ab}^{-1}(i\omega_n = 0), \quad (16)$$

where M_a is the mass of atom a (recall that a is a combined index labelling atoms and Cartesian directions). As mentioned above, this is true for the SCHA free energy landscape⁴⁰. In the following, we extend the proof in the exact case, too.

From the Kubo's equation, Green's function is defined as

$$G_{ab}(\tau) = -\sqrt{M_a M_b} \langle T_\tau [\hat{u}_a(\tau) \hat{u}_b(0)] \rangle_\rho, \quad (17)$$

where the displacement operator \hat{u} is measured from the equilibrium average position $\mathcal{R}_a^{\text{eq}}$, that is, $\hat{u}_a(\tau) = \hat{R}_a(\tau) - \mathcal{R}_a^{\text{eq}}$, where τ is the imaginary time, T_τ is the time-ordering operator and $\hat{\rho} = e^{-\beta\hat{H}}/Z$ is the density matrix. The partition function is $Z = \text{Tr}[e^{-\beta\hat{H}}]$, where \hat{H} is the Hamiltonian of the system. The Lehmann representation of Green's function in the Matsubara frequency domain⁵⁴ is given by:

$$\frac{G_{ab}(i\omega_n)}{\sqrt{M_a M_b}} = \frac{1}{Z} \sum_{nm} \frac{e^{-\beta E_n} - e^{-\beta E_m}}{i\omega_n + E_n - E_m} \times \langle \psi_n | (\hat{R}_a - \mathcal{R}_a^{\text{eq}}) | \psi_m \rangle \langle \psi_m | (\hat{R}_b - \mathcal{R}_b^{\text{eq}}) | \psi_n \rangle. \quad (18)$$

At $T = 0$ K, the static limit of Green's function can be simply written as

$$\frac{G_{ab}}{\sqrt{M_a M_b}} = \sum_m \frac{1}{E_0 - E_m} [\langle \psi_0 | (\hat{R}_a - \mathcal{R}_a^{\text{eq}}) | \psi_m \rangle \langle \psi_m | (\hat{R}_b - \mathcal{R}_b^{\text{eq}}) | \psi_0 \rangle] + \sum_m \frac{1}{E_0 - E_m} [\langle \psi_0 | (\hat{R}_b - \mathcal{R}_b^{\text{eq}}) | \psi_m \rangle \langle \psi_m | (\hat{R}_a - \mathcal{R}_a^{\text{eq}}) | \psi_0 \rangle], \quad (19)$$

where $|\psi_n\rangle$ and E_n are the eigenvectors and eigenvalues of the Hamiltonian \hat{H} , that is,

$$\hat{H}|\psi_n\rangle = E_n |\psi_n\rangle, \quad (20)$$

and $|\psi_0\rangle$ and E_0 are the corresponding ground-state eigenvectors and eigenenergies, respectively. Considering that at equilibrium $\langle \psi_0 | (\hat{R}_a - \mathcal{R}_a^{\text{eq}}) | \psi_0 \rangle = 0$, we can safely ignore the $m = 0$ term in the sum. In this way, the zero-temperature static limit of Green's function can be written as

$$\frac{G_{ab}}{\sqrt{M_a M_b}} = \sum_{m \neq 0} \frac{1}{E_0 - E_m} [\langle \psi_0 | (\hat{R}_a - \mathcal{R}_a^{\text{eq}}) | \psi_m \rangle \langle \psi_m | (\hat{R}_b - \mathcal{R}_b^{\text{eq}}) | \psi_0 \rangle] + \sum_{m \neq 0} \frac{1}{E_0 - E_m} [\langle \psi_0 | (\hat{R}_b - \mathcal{R}_b^{\text{eq}}) | \psi_m \rangle \langle \psi_m | (\hat{R}_a - \mathcal{R}_a^{\text{eq}}) | \psi_0 \rangle]. \quad (21)$$

To perform similar operations on the left-hand side of equation (16), we define the positional free energy landscape at $T = 0$ K as the energy of the system when the average position of the atoms is constrained to \mathcal{R} as

$$E(\mathcal{R}) = \min_{\psi_0} \left\{ \langle \psi_0 | \hat{H} | \psi_0 \rangle + \sum_a \lambda_a (\langle \psi_0 | \hat{R}_a | \psi_0 \rangle - \mathcal{R}_a) \right\}, \quad (22)$$

where the constraint of the average position is obtained owing to the Lagrange multiplier λ_a , which needs to be optimized. Indeed, when \mathcal{R} is equal to the equilibrium average positions of the atoms, we recover the standard definition of the ground-state energy in quantum mechanics:

$$E = \min_{\psi_0} \{ \langle \psi_0 | \hat{H} | \psi_0 \rangle \}. \quad (23)$$

We notice that a small perturbation of the energy landscape from equilibrium $\mathcal{R}_a = \mathcal{R}_a^{\text{eq}} + \delta\mathcal{R}_a$ is equivalent to perturbing the Hamiltonian with an external potential of the form

$$\delta\hat{V} = \sum_a \lambda_a (\hat{R}_a - \mathcal{R}_a), \quad (24)$$

where λ acts as the small parameter that controls the perturbation and is of the order of $\delta\mathcal{R}$.

The solution of equation (22) yields a new ground state $\tilde{\psi}_0$ different from ψ_0 , with $\lambda \neq 0$. By construction, we know that

$$\delta\mathcal{R}_a = \langle \tilde{\psi}_0 | (\hat{R}_a - \mathcal{R}_a^{\text{eq}}) | \tilde{\psi}_0 \rangle, \quad (25)$$

where $|\tilde{\psi}_n\rangle$ are the eigenfunctions of the perturbed Hamiltonian. At the lowest order in λ , this expression becomes

$$\delta\mathcal{R}_a = \left[\langle \psi_0 | (\hat{R}_a - \mathcal{R}_a^{\text{eq}}) | \psi_0 \rangle + \langle \psi_0 | (\hat{R}_a - \mathcal{R}_a^{\text{eq}}) | \psi_0^{(1)} \rangle \right], \quad (26)$$

where $|\psi_0^{(1)}\rangle$ is the first-order change in the ground-state eigenfunction. Making use of perturbation theory, we get

$$|\psi_0^{(1)}\rangle = \sum_{m \neq 0} \frac{\langle \psi_m | \delta\hat{V} | \psi_0 \rangle}{E_0 - E_m} |\psi_m\rangle, \quad (27)$$

and thus,

$$\delta\mathcal{R}_a = \sum_b \lambda_b \sum_{m \neq 0} \left[\frac{1}{E_0 - E_m} \langle \psi_0 | (\hat{R}_a - \mathcal{R}_a^{\text{eq}}) | \psi_m \rangle \langle \psi_m | (\hat{R}_b - \mathcal{R}_b^{\text{eq}}) | \psi_0 \rangle + \frac{1}{E_0 - E_m} \langle \psi_0 | (\hat{R}_b - \mathcal{R}_b^{\text{eq}}) | \psi_m \rangle \langle \psi_m | (\hat{R}_a - \mathcal{R}_a^{\text{eq}}) | \psi_0 \rangle \right]. \quad (28)$$

Comparing with equation (21), we deduce the important

$$\delta\mathcal{R}_a = \sum_b \lambda_b \frac{G_{ab}}{\sqrt{M_a M_b}} \quad (29)$$

relation. Inverting this relation, we obtain

$$\lambda_a = \sum_b \sqrt{M_a M_b} G_{ab}^{-1} \delta\mathcal{R}_b, \quad (30)$$

which determines the relation between the Lagrange multipliers and the shift in the average position.

To estimate the free energy Hessian when the average position is forced to shift from the equilibrium position, we will also assume perturbation theory. Thus,

$$E(\mathcal{R} + \delta\mathcal{R}) = E(\mathcal{R}^{\text{eq}}) + \langle \tilde{\psi}_0 | \hat{H} | \tilde{\psi}_0 \rangle. \quad (31)$$

Considering that the linear order term vanishes, we need to go to the second order to have a non-vanishing contribution:

$$E(\mathcal{R} + \delta\mathcal{R}) = E(\mathcal{R}^{\text{eq}}) + \langle \tilde{\psi}_0^{(2)} | \hat{H} | \tilde{\psi}_0^{(2)} \rangle + \langle \tilde{\psi}_0^{(1)} | \hat{H} | \tilde{\psi}_0^{(1)} \rangle + \langle \tilde{\psi}_0^{(1)} | \hat{H} | \tilde{\psi}_0^{(2)} \rangle + \langle \tilde{\psi}_0^{(2)} | \hat{H} | \tilde{\psi}_0^{(1)} \rangle. \quad (32)$$

Considering that the second-order change in the wavefunction is given by

$$|\tilde{\psi}_0^{(2)}\rangle = \sum_{m,l,m \neq 0,l \neq 0} \frac{\langle \psi_l | \delta\hat{V} | \psi_m \rangle \langle \psi_m | \delta\hat{V} | \psi_0 \rangle}{(E_0 - E_m)(E_0 - E_l)} |\psi_l\rangle - \sum_{m,m \neq 0} \frac{\langle \psi_m | \delta\hat{V} | \psi_0 \rangle \langle \psi_0 | \delta\hat{V} | \psi_0 \rangle}{(E_0 - E_m)^2} |\psi_m\rangle - \frac{1}{2} |\psi_0\rangle + \sum_{m,m \neq 0} \frac{|\langle \psi_m | \delta\hat{V} | \psi_0 \rangle|^2}{(E_0 - E_m)^2}, \quad (33)$$

we obtain

$$\begin{aligned} E(\mathcal{R} + \delta\mathcal{R}) &= E(\mathcal{R}^{\text{eq}}) - \sum_{m \neq 0} E_0 \frac{|\langle \psi_m | \delta\hat{V} | \psi_0 \rangle|^2}{(E_0 - E_m)^2} + \sum_{m \neq 0} E_m \frac{|\langle \psi_m | \delta\hat{V} | \psi_0 \rangle|^2}{(E_0 - E_m)^2} \\ &= E(\mathcal{R}^{\text{eq}}) - \sum_{m \neq 0} \frac{|\langle \psi_m | \delta\hat{V} | \psi_0 \rangle|^2}{(E_0 - E_m)} \\ &= E(\mathcal{R}^{\text{eq}}) - \sum_{ab} \lambda_a \lambda_b \sum_{m \neq 0} \frac{1}{(E_0 - E_m)} \\ &\quad \langle \psi_0 | (\hat{R}_a - \mathcal{R}_a^{\text{eq}}) | \psi_m \rangle \langle \psi_m | (\hat{R}_b - \mathcal{R}_b^{\text{eq}}) | \psi_0 \rangle \\ &= E(\mathcal{R}^{\text{eq}}) - \frac{1}{2} \sum_{ab} \lambda_a \lambda_b \frac{G_{ab}}{\sqrt{M_a M_b}}. \end{aligned} \quad (34)$$

Making use of equation (30), we finally obtain

$$E(\mathcal{R} + \delta\mathcal{R}) = E(\mathcal{R}^{\text{eq}}) - \frac{1}{2} \sum_{ab} \sqrt{M_a M_b} G_{ab}^{-1} \delta\mathcal{R}_a \delta\mathcal{R}_b, \quad (35)$$

which proves equation (16) in the $T = 0$ K case, that is, it shows that for any static theory, the physical phonons coincide with the eigenvalues of the free energy Hessian.

Empirical potential benchmark and calculation parameters of atomistic calculations

For calculating the forces needed in the atomistic SCHA minimization⁴¹, we have used an empirical potential trained with machine-learning and density functional theory (DFT) forces. The details about the machine-learning training are explained elsewhere⁴³. Here we have benchmarked the ability of the potential to account for anharmonic effects. Therefore, we have applied the SCHA method by using DFT and empirical forces in a 2×2 supercell and we have checked the anharmonic effects in the optical modes at the Γ point. The machine-learning potential is trained with an exchange–correlation functional⁵⁵. For the DFT calculations, we have applied a Perdew–Burke–Ernzerhof⁵⁶ ultrasoft pseudopotential⁵⁷ with van der Waals corrections⁵⁸. Extended Data Figs. 4 and 5 show the results. Extended Data Fig. 4 shows that the two potentials provide very similar harmonic phonons. Due to the different exchange–correlation functional, there is a slight offset (Extended Data Fig. 5); however, the anharmonic lineshifts are very well captured within the empirical potential. For the self-consistent DFT calculations used in the benchmark, we have used a plane-wave cutoff of 70 Ry and a 700 Ry cutoff for the density. For the Brillouin-zone integration, we have used a Monkhorst–Pack grid⁵⁹ of 32×32 points with a Gaussian smearing of 0.02 Ry.

The atomistic calculations of the linewidth in the main text have been performed with a grid of 400×400 momentum points for the bubble self-energy, with a Gaussian smearing (δ) of 1 cm^{-1} . For the stress calculation to account for thermal expansion, we have used a 10×10 supercell. We have used the same supercell for the SCHA auxiliary and physical frequency calculations in the atomistic case. For the linewidth calculations, we have used $\Phi^{(3)}$ calculated in a 3×3 supercell and Fourier interpolated it. We have tested all the calculations with denser grids and bigger supercells.

SCHA applied to the continuum membrane Hamiltonian

The general rotationally invariant potential for a membrane can be written as follows:

$$V = \frac{1}{2} \int_{\Omega} d^2x \left(\kappa (\partial^2 h)^2 + \sum_{n \geq 2} u_{i_1 j_1} \dots u_{i_n j_n} C_{i_1 j_1 \dots i_n j_n}^{(2n)} \right), \quad (36)$$

where Ω is the area of the membrane in equilibrium, κ is the bending rigidity, h is the out-of-plane component of the displacement field and the rotationally invariant strain tensor u_{ij} is defined using the in-plane displacement field u_i , namely,

$$u_{ij} = \frac{1}{2} (\partial_i u_j + \partial_j u_i + \partial_i \mathbf{u} \cdot \partial_j \mathbf{u} + \partial_i h \partial_j h). \quad (37)$$

Here $C_{i_1 j_1 \dots i_n j_n}^{(2n)}$ is the generic elastic tensor of rank $2n$. In the previous expression, the subscripts label the 2D coordinates x and y and the sum over the indices is assumed. The second-order expansion of equation (36) with respect to the phonon fields is given by

$$V = \frac{1}{2} \int_{\Omega} d^2x \left(\kappa (\partial^2 h)^2 + C_{ijkl}^{(4)} u_{ij} u_{kl} \right), \quad (38)$$

where $C_{ijkl}^{(4)} = \lambda \delta_{ij} \delta_{kl} + \mu (\delta_{ik} \delta_{jl} + \delta_{il} \delta_{jk})$. By using equation (37) and $C_{ijkl}^{(4)} = C_{ijkl}^{(4)}$, equation (38) can be rewritten as

$$V = \frac{1}{2} \int_{\Omega} d^2x \left[\kappa (\partial^2 h)^2 + C_{ijkl}^{(4)} \partial_i u_j \partial_k u_l + C_{ijkl}^{(4)} \partial_i u_j \partial_k h \partial_l h + \frac{C_{ijkl}^{(4)}}{4} \partial_i h \partial_j h \partial_k h \partial_l h + \frac{C_{ijkl}^{(4)}}{2} \partial_i \mathbf{u} \cdot \partial_j \mathbf{u} \partial_k h \partial_l h + C_{ijkl}^{(4)} \partial_i u_j \partial_k \mathbf{u} \cdot \partial_l \mathbf{u} + \frac{C_{ijkl}^{(4)}}{4} \partial_i \mathbf{u} \cdot \partial_j \mathbf{u} \partial_k \mathbf{u} \cdot \partial_l \mathbf{u} \right]. \quad (39)$$

If we allow the lattice spacing a to be a variable, we can vary it by simply shifting the derivatives of the in-plane displacements according to $\partial_i u_j \rightarrow \partial_i u_j + \delta^j \delta a$, where $\delta a = (a - a_0)/a_0$. Then, by taking into account periodic boundary conditions as $\int_{\Omega} d^2x \partial_i u_j = 0$, we can rewrite the potential as

$$\begin{aligned} V \rightarrow V + 2\Omega(1 + \delta a)(\lambda + \mu)\delta a^2 + \\ + \left(1 + \frac{\delta a}{2}\right) \delta a(\lambda + \mu) \int_{\Omega} d^2x \partial_k h \partial_k h + \\ + \frac{\delta a}{2} \int_{\Omega} d^2x C_{ijkl}^{(4)} \partial_i u_j \partial_k h \partial_l h + \\ + \left(1 + \frac{\delta a}{2}\right) \delta a \int_{\Omega} d^2x C_{ijkl}^{(4)} \partial_i u_j \partial_k u_l + \\ + \left(1 + \frac{\delta a}{2}\right) \delta a(\lambda + \mu) \int_{\Omega} d^2x \partial_k \mathbf{u} \cdot \partial_k \mathbf{u} + \frac{\delta a^4 \Omega}{2} (\lambda + \mu) + \\ + \frac{\delta a}{4} \int_{\Omega} d^2x C_{ijkl}^{(4)} [\partial_i \mathbf{u} \cdot \partial_j \mathbf{u} \partial_k u_l + \partial_i u_j \partial_k \mathbf{u} \cdot \partial_l \mathbf{u}]. \end{aligned} \quad (40)$$

The displacement fields $\mathbf{u}(\mathbf{x})$ and $h(\mathbf{x})$ can be expanded in the following plane-wave basis set:

$$\mathbf{u}(\mathbf{x}) = \frac{1}{\sqrt{\Omega}} \sum_{\mathbf{q}} \mathbf{u}(\mathbf{q}) e^{i\mathbf{q} \cdot \mathbf{x}}, \quad (41)$$

$$h(\mathbf{x}) = \frac{1}{\sqrt{\Omega}} \sum_{\mathbf{q}} h(\mathbf{q}) e^{i\mathbf{q} \cdot \mathbf{x}}, \quad (42)$$

where \mathbf{q} are discrete wavevectors determined by periodic boundary conditions and $\mathbf{u}(\mathbf{q})$ and $h(\mathbf{q})$ are the corresponding Fourier transforms, which are defined as follows:

$$\mathbf{u}(\mathbf{q}) = \frac{1}{\sqrt{\Omega}} \int_{\Omega} d^2x \mathbf{u}(\mathbf{x}) e^{-i\mathbf{q} \cdot \mathbf{x}}, \quad (43)$$

$$h(\mathbf{q}) = \frac{1}{\sqrt{\Omega}} \int_{\Omega} d^2x h(\mathbf{x}) e^{-i\mathbf{q} \cdot \mathbf{x}}. \quad (44)$$

Then, the SCHA free energy can be written as (we use $\hbar = k_B = 1$)

$$\begin{aligned} \mathcal{F}(V) = F_V + 2\Omega \left(1 + \delta a + \frac{\delta a^2}{4} \right) (\lambda + \mu) \delta a^2 + \\ + \frac{1}{2} \sum_{\mathbf{q}} \left\{ g[\omega_{\text{SCHA}}^{(h)}(\mathbf{q})] \kappa |\mathbf{q}|^4 + \right. \\ + \{ (\lambda + 2\mu) g[\omega_{\text{SCHA}}^{(\text{LA})}(\mathbf{q})] + \mu g[\omega_{\text{SCHA}}^{(\text{TA})}(\mathbf{q})] \} |\mathbf{q}|^2 + \\ + \frac{\lambda + 2\mu}{4\Omega} \sum_{\mathbf{k}} g[\omega_{\text{SCHA}}^{(h)}(\mathbf{q})] g[\omega_{\text{SCHA}}^{(h)}(\mathbf{k})] [|\mathbf{q}|^2 |\mathbf{k}|^2 + 2(\mathbf{q} \cdot \mathbf{k})^2] + \\ + \frac{1}{2\Omega} \sum_{\mathbf{k}} g[\omega_{\text{SCHA}}^{(h)}(\mathbf{k})] \{ g[\omega_{\text{SCHA}}^{(\text{LA})}(\mathbf{q})] + g[\omega_{\text{SCHA}}^{(\text{TA})}(\mathbf{q})] \} \times \\ \times [|\mathbf{q}|^2 |\mathbf{k}|^2 + 2\mu(\mathbf{q} \cdot \mathbf{k})^2] + \\ + 2 \left(1 + \frac{\delta a}{2} \right) \delta a (\lambda + \mu) g[\omega_{\text{SCHA}}^{(h)}(\mathbf{q})] |\mathbf{q}|^2 + \\ + 2 \left(1 + \frac{\delta a}{2} \right) \delta a \{ (\lambda + 2\mu) g[\omega_{\text{SCHA}}^{(\text{LA})}(\mathbf{q})] + \mu g[\omega_{\text{SCHA}}^{(\text{TA})}(\mathbf{q})] \} |\mathbf{q}|^2 + \\ + 2 \left(1 + \frac{\delta a}{2} \right) \delta a (\lambda + \mu) \{ g[\omega_{\text{SCHA}}^{(\text{LA})}(\mathbf{q})] + g[\omega_{\text{SCHA}}^{(\text{TA})}(\mathbf{q})] \} |\mathbf{q}|^2 + \\ + \frac{1}{4\Omega} \sum_{\mathbf{k}} \left\{ 4 g[\omega_{\text{SCHA}}^{(\text{LA})}(\mathbf{q})] g[\omega_{\text{SCHA}}^{(\text{TA})}(\mathbf{k})] \times \right. \\ \times [\lambda(\mathbf{q} \cdot \mathbf{k})^2 + \mu |\mathbf{q}|^2 |\mathbf{k}|^2 + \mu(\mathbf{q} \cdot \mathbf{k})^2] (\hat{\mathbf{q}}_{\perp} \cdot \hat{\mathbf{k}}) + \\ + 2 g[\omega_{\text{SCHA}}^{(\text{LA})}(\mathbf{q})] g[\omega_{\text{SCHA}}^{(\text{TA})}(\mathbf{k})] [\lambda |\mathbf{q}|^2 |\mathbf{k}|^2 + 2\mu(\mathbf{q} \cdot \mathbf{k})^2] + \\ + (g[\omega_{\text{SCHA}}^{(\text{LA})}(\mathbf{q})] g[\omega_{\text{SCHA}}^{(\text{LA})}(\mathbf{k})] + g[\omega_{\text{SCHA}}^{(\text{TA})}(\mathbf{q})] g[\omega_{\text{SCHA}}^{(\text{TA})}(\mathbf{k})]) \times \\ \times [|\mathbf{q}|^2 |\mathbf{k}|^2 + 2\mu(\mathbf{q} \cdot \mathbf{k})^2] + \\ + 2 (g[\omega_{\text{SCHA}}^{(\text{LA})}(\mathbf{q})] g[\omega_{\text{SCHA}}^{(\text{LA})}(\mathbf{k})]) \times \\ \times [\lambda(\mathbf{q} \cdot \mathbf{k})^2 + \mu |\mathbf{q}|^2 |\mathbf{k}|^2 + \mu(\mathbf{q} \cdot \mathbf{k})^2] (\hat{\mathbf{q}} \cdot \hat{\mathbf{k}}) + \\ + 2 (g[\omega_{\text{SCHA}}^{(\text{TA})}(\mathbf{q})] g[\omega_{\text{SCHA}}^{(\text{TA})}(\mathbf{k})]) \times \\ \times [\lambda(\mathbf{q} \cdot \mathbf{k})^2 + \mu |\mathbf{q}|^2 |\mathbf{k}|^2 + \mu(\mathbf{q} \cdot \mathbf{k})^2] (\hat{\mathbf{q}}_{\perp} \cdot \hat{\mathbf{k}}_{\perp}) \left. \right\} + \\ - \sum_{\alpha} g[\omega_{\text{SCHA}}^{(\alpha)}(\mathbf{q})] \Phi_{\text{SCHA}}^{(\alpha)}(\mathbf{q}) \left. \right\}. \end{aligned} \quad (45)$$

where $g(\omega) = \coth((\omega/2T))/(2\rho\omega)$ and $\omega_{\text{SCHA}}^{\alpha}(\mathbf{q}) = \sqrt{\Phi_{\text{SCHA}}^{(\alpha)}(\mathbf{q})}/\rho$ ($\alpha = h, \text{LA}, \text{TA}$) is the SCHA auxiliary frequency. Also, ρ is the mass density. In equation (45), the in-plane displacement vector $\mathbf{u}(\mathbf{q})$ is separated into longitudinal and transversal components, that is, $\mathbf{u}(\mathbf{q}) = u_{\text{LA}}(\mathbf{q})\hat{\mathbf{q}} + u_{\text{TA}}(\mathbf{q})\hat{\mathbf{q}}_{\perp}$, where $\hat{\mathbf{q}}_{\perp}$ is the unitary vector perpendicular to $\hat{\mathbf{q}}$. Furthermore, F_{ν} is the harmonic free energy of the harmonic auxiliary potential ν . Now, by taking the derivative of the SCHA free energy with respect to the lattice constant and SCHA auxiliary frequencies, we arrive at the following SCHA equations:

$$\begin{aligned} \frac{\partial \mathcal{F}(\nu)}{\partial \delta a} = 0 = & 2\Omega(2\delta a + 3\delta a^2 + \delta a^3)(\lambda + \mu) + \\ & + \frac{1}{2} \sum_{\mathbf{q}} g[\omega_{\text{SCHA}}^{(h)}(\mathbf{q})] 2(1 + \delta a)(\lambda + \mu)|\mathbf{q}|^2 + \\ & + \frac{1}{2} \sum_{\mathbf{q}} g[\omega_{\text{SCHA}}^{(\text{LA})}(\mathbf{q})] [2(1 + \delta a)(\lambda + 2\mu)|\mathbf{q}|^2 + 2(1 + \delta a)(\lambda + \mu)|\mathbf{q}|^2] + \\ & + \frac{1}{2} \sum_{\mathbf{q}} g[\omega_{\text{SCHA}}^{(\text{TA})}(\mathbf{q})] [2(1 + \delta a)\mu|\mathbf{q}|^2 + 2(1 + \delta a)(\lambda + \mu)|\mathbf{q}|^2], \end{aligned} \quad (46)$$

$$\begin{aligned} \Phi_{\text{SCHA}}^{(h)}(\mathbf{q}) = & \kappa|\mathbf{q}|^4 + 2(1 + \delta a/2)\delta a(\lambda + \mu)|\mathbf{q}|^2 + \\ & + \frac{\lambda + 2\mu}{2\Omega} \sum_{\mathbf{k}} g[\omega_{\text{SCHA}}^{(h)}(\mathbf{k})] [|\mathbf{q}|^2|\mathbf{k}|^2 + 2(\mathbf{q} \cdot \mathbf{k})^2] + \\ & + \frac{1}{2\Omega} \sum_{\mathbf{k}} \{g[\omega_{\text{SCHA}}^{(\text{LA})}(\mathbf{k})] + g[\omega_{\text{SCHA}}^{(\text{TA})}(\mathbf{k})]\} [\lambda|\mathbf{q}|^2|\mathbf{k}|^2 + 2\mu(\mathbf{q} \cdot \mathbf{k})^2], \end{aligned} \quad (47)$$

$$\begin{aligned} \Phi_{\text{SCHA}}^{(\text{LA})}(\mathbf{q}) = & (\lambda + 2\mu)|\mathbf{q}|^2 + 2(1 + \delta a/2)\delta a(\lambda + 2\mu)|\mathbf{q}|^2 + \\ & + 2(1 + \delta a/2)\delta a(\lambda + \mu)|\mathbf{q}|^2 + \\ & + \frac{1}{2\Omega} \sum_{\mathbf{k}} g[\omega_{\text{SCHA}}^{(h)}(\mathbf{k})] [\lambda|\mathbf{q}|^2|\mathbf{k}|^2 + 2\mu(\mathbf{q} \cdot \mathbf{k})^2] + \\ & + \frac{1}{4\Omega} \sum_{\mathbf{k}} \{4g[\omega_{\text{SCHA}}^{(\text{TA})}(\mathbf{k})] [\lambda(\mathbf{q} \cdot \mathbf{k})^2 + \mu|\mathbf{q}|^2|\mathbf{k}|^2 + \mu(\mathbf{q} \cdot \mathbf{k})^2](\hat{\mathbf{q}}_{\perp} \cdot \hat{\mathbf{k}}) + \\ & + 2g[\omega_{\text{SCHA}}^{(\text{TA})}(\mathbf{k})] [\lambda|\mathbf{q}|^2|\mathbf{k}|^2 + 2\mu(\mathbf{q} \cdot \mathbf{k})^2] + \\ & + 2g[\omega_{\text{SCHA}}^{(\text{LA})}(\mathbf{k})] [\lambda|\mathbf{q}|^2|\mathbf{k}|^2 + 2\mu(\mathbf{q} \cdot \mathbf{k})^2] + \\ & + 4g[\omega_{\text{SCHA}}^{(\text{LA})}(\mathbf{k})] [\lambda(\mathbf{q} \cdot \mathbf{k})^2 + \mu|\mathbf{q}|^2|\mathbf{k}|^2 + \mu(\mathbf{q} \cdot \mathbf{k})^2](\hat{\mathbf{q}}_{\perp} \cdot \hat{\mathbf{k}})\} \end{aligned} \quad (48)$$

and

$$\begin{aligned} \Phi_{\text{SCHA}}^{(\text{TA})}(\mathbf{q}) = & \mu|\mathbf{q}|^2 + 2(1 + \delta a/2)\delta a\mu|\mathbf{q}|^2 + \\ & + 2(1 + \delta a/2)\delta a(\lambda + \mu)|\mathbf{q}|^2 + \\ & + \frac{1}{2\Omega} \sum_{\mathbf{k}} g[\omega_{\text{SCHA}}^{(h)}(\mathbf{k})] [\lambda|\mathbf{q}|^2|\mathbf{k}|^2 + 2\mu(\mathbf{q} \cdot \mathbf{k})^2] + \\ & + \frac{1}{4\Omega} \sum_{\mathbf{k}} \{4g[\omega_{\text{SCHA}}^{(\text{TA})}(\mathbf{k})] [\lambda(\mathbf{q} \cdot \mathbf{k})^2 + \mu|\mathbf{q}|^2|\mathbf{k}|^2 + \mu(\mathbf{q} \cdot \mathbf{k})^2](\hat{\mathbf{q}}_{\perp} \cdot \hat{\mathbf{k}}_{\perp}) + \\ & + 4g[\omega_{\text{SCHA}}^{(\text{LA})}(\mathbf{k})] [\lambda(\mathbf{q} \cdot \mathbf{k})^2 + \mu|\mathbf{q}|^2|\mathbf{k}|^2 + \mu(\mathbf{q} \cdot \mathbf{k})^2](\hat{\mathbf{q}}_{\perp} \cdot \hat{\mathbf{k}}) + \\ & + 2g[\omega_{\text{SCHA}}^{(\text{TA})}(\mathbf{k})] [\lambda|\mathbf{q}|^2|\mathbf{k}|^2 + 2\mu(\mathbf{q} \cdot \mathbf{k})^2]\}. \end{aligned} \quad (49)$$

When solving this set of equations, it has been taken into account that the assumed periodic boundary conditions make the reciprocal space discrete. To reach wavevectors that are a magnitude of order smaller than in our atomistic calculations, we have worked with a square membrane of size $L_x = L_y = \frac{2\pi}{0.01} \text{ \AA}$. On the other side, the implicit continuity of the membrane Hamiltonian makes Fourier transforms to be non-periodic. Then, as displacement fields $\mathbf{u}(\mathbf{x})$ and $h(\mathbf{x})$ are smooth functions in real space, their discrete and non-periodic Fourier transforms $\mathbf{u}(\mathbf{q})$ and $h(\mathbf{q})$ (and related magnitudes) are expected to rapidly decay in reciprocal space. Therefore, we can converge our results with

respect to a cutoff radius in momentum space, consequently defining a circular grid. The value of this cutoff radius is temperature dependent, because modes with greater q values are thermally excited when increasing the temperature. We have found that with a value of $R_{\text{cut}} = 0.8 \text{ \AA}^{-1}$, convergence is achieved for temperatures close to 0 K. This radius encloses 20,080 \mathbf{q} points, which yields a total of 60,241 coupled equations that we have solved by applying the Newton–Raphson method⁶⁰. This model accounts for the negative thermal expansion of graphene (Extended Data Fig. 6).

Regarding the second derivative of the free energy, namely, the physical phonons in the static approach, the most general formula for the correction to the SCHA auxiliary phonon frequencies is

$$\begin{aligned} D_{\alpha\beta}^{\text{corr}}(-\mathbf{q}, \mathbf{q}) = & \sum_{\gamma\delta\epsilon\zeta} \sum_{\mathbf{p}\mathbf{k}} D_{\alpha\gamma\delta}^{(3)}(-\mathbf{q}, \mathbf{p}, \mathbf{q} - \mathbf{p}) \times \\ & \times [1 - D_{\gamma\delta\epsilon\zeta}^{(4)}(-\mathbf{p}, \mathbf{p} - \mathbf{q}, \mathbf{k}, \mathbf{q} - \mathbf{k})]^{-1} D_{\epsilon\zeta\beta}^{(3)}(-\mathbf{k}, \mathbf{k} - \mathbf{q}, \mathbf{q}), \end{aligned} \quad (50)$$

where the subindexes run on the normal coordinates $\alpha, \beta, \gamma, \delta, \epsilon, \zeta = h, u_{\text{LA}}$ and u_{TA} , and the dynamical matrices in normal coordinates are defined as

$$D_{\alpha\beta\gamma}^{(3)}(\mathbf{q}, \mathbf{k}, \mathbf{p}) = \frac{1}{\rho^{3/2}} \left\langle \frac{\partial^3 V}{\partial \alpha(\mathbf{q}) \partial \beta(\mathbf{k}) \partial \gamma(\mathbf{p})} \right\rangle_{\rho_{\nu}} \sqrt{G_{\beta\gamma}(\mathbf{k}, \mathbf{p})}, \quad (51)$$

$$\begin{aligned} D_{\alpha\beta\gamma\epsilon}^{(4)}(\mathbf{q}, \mathbf{q}', \mathbf{k}, \mathbf{k}') = & \frac{1}{\rho^2} \left\langle \frac{\partial^4 V}{\partial \alpha(\mathbf{q}) \partial \beta(\mathbf{q}') \partial \gamma(\mathbf{k}) \partial \epsilon(\mathbf{k}')} \right\rangle_{\rho_{\nu}} \\ & \times \sqrt{G_{\alpha\beta}(\mathbf{q}, \mathbf{k}) G_{\gamma\epsilon}(\mathbf{q}', \mathbf{k}')}. \end{aligned} \quad (52)$$

The matrix $G_{\alpha\beta}(\mathbf{q}, \mathbf{k})$ is defined as

$$G_{\alpha\beta}(\mathbf{q}, \mathbf{k}) = \frac{\bar{F}(0, \omega_{\text{SCHA}}^{\alpha}(\mathbf{q}), \omega_{\text{SCHA}}^{\beta}(\mathbf{k}))}{\omega_{\text{SCHA}}^{\alpha}(\mathbf{q}) \omega_{\text{SCHA}}^{\beta}(\mathbf{k})}, \quad (53)$$

where $\bar{F}(0, \omega_{\text{SCHA}}^{\alpha}(\mathbf{q}), \omega_{\text{SCHA}}^{\beta}(\mathbf{k}))$ is the function defined in equation (9). We are interested in the corrections to the out-of-plane modes; therefore, we are interested in the terms of the type

$$\begin{aligned} D_{hh}^{\text{corr}}(-\mathbf{q}, \mathbf{q}) = & \sum_{\gamma\delta\epsilon\zeta} \sum_{\mathbf{p}\mathbf{k}} D_{h\gamma\delta}^{(3)}(-\mathbf{q}, \mathbf{p}, \mathbf{q} - \mathbf{p}) \times \\ & \times [1 - D_{\gamma\delta\epsilon\zeta}^{(4)}(-\mathbf{p}, \mathbf{p} - \mathbf{q}, \mathbf{k}, \mathbf{q} - \mathbf{k})]^{-1} D_{\epsilon\zeta h}^{(3)}(-\mathbf{k}, \mathbf{k} - \mathbf{q}, \mathbf{q}). \end{aligned} \quad (54)$$

By looking at equation (40), we can see that only the terms of the type $\int d^2x C^{ijkl} \partial_i u_j \partial_k h \partial_l h$ will contribute to the statistical average in equation (51). Therefore, equation (50) can be rewritten as

$$\begin{aligned} D_{hh}^{\text{corr}}(-\mathbf{q}, \mathbf{q}) = & 4 \sum_{\alpha\beta} \sum_{\mathbf{p}\mathbf{k}} D_{h\alpha\beta}^{(3)}(-\mathbf{q}, \mathbf{p}, \mathbf{q} - \mathbf{p}) \times \\ & \times [1 - D_{h\alpha\beta}^{(4)}(-\mathbf{p}, \mathbf{p} - \mathbf{q}, \mathbf{k}, \mathbf{q} - \mathbf{k})]^{-1} D_{h\beta h}^{(3)}(-\mathbf{k}, \mathbf{k} - \mathbf{q}, \mathbf{q}), \end{aligned} \quad (55)$$

where the subindexes now only run in $\alpha, \beta = u_{\text{LA}}, u_{\text{TA}}$. Now, we can calculate the statistical averages as follows:

$$\begin{aligned} \left\langle \frac{\partial^3 V}{\partial h(\mathbf{k}_1) \partial h(\mathbf{k}_2) \partial u_{\text{LA}}(\mathbf{k}_3)} \right\rangle_{\rho_{\nu}} = & \frac{1 + \delta a}{\sqrt{\Omega}} \delta_{\mathbf{k}_1 + \mathbf{k}_2 + \mathbf{k}_3, 0} \times \\ & \times \left[\lambda |\mathbf{k}_3| \mathbf{k}_1 \cdot \mathbf{k}_2 + 2\mu \frac{(\mathbf{k}_3 \cdot \mathbf{k}_1)(\mathbf{k}_3 \cdot \mathbf{k}_2)}{|\mathbf{k}_3|} \right], \end{aligned} \quad (56)$$

$$\begin{aligned} \left\langle \frac{\partial^3 V}{\partial h(\mathbf{k}_1) \partial h(\mathbf{k}_2) \partial u_{\text{TA}}(\mathbf{k}_3)} \right\rangle_{\rho_{\nu}} = & \frac{\mu(1 + \delta a)}{\sqrt{\Omega}} \delta_{\mathbf{k}_1 + \mathbf{k}_2 + \mathbf{k}_3, 0} \times \\ & \times \left[\frac{(\mathbf{k}_3 \cdot \mathbf{k}_1)(\mathbf{k}_{3\perp} \cdot \mathbf{k}_2) + (\mathbf{k}_3 \cdot \mathbf{k}_2)(\mathbf{k}_{3\perp} \cdot \mathbf{k}_1)}{|\mathbf{k}_3|} \right], \end{aligned} \quad (57)$$

$$\begin{aligned} & \left\langle \frac{\partial^4 V}{\partial h(\mathbf{k}_1) \partial h(\mathbf{k}_2) \partial u_{LA}(\mathbf{k}_3) \partial u_{LA}(\mathbf{k}_4)} \right\rangle_{\rho_V} \\ &= \frac{1}{\Omega} \delta_{\mathbf{k}_1+\mathbf{k}_2+\mathbf{k}_3+\mathbf{k}_4,0} \frac{\mathbf{k}_3 \cdot \mathbf{k}_4}{|\mathbf{k}_3||\mathbf{k}_4|} [\lambda(\mathbf{k}_3 \cdot \mathbf{k}_4)(\mathbf{k}_1 \cdot \mathbf{k}_2) + \\ & \quad + \mu(\mathbf{k}_3 \cdot \mathbf{k}_1)(\mathbf{k}_4 \cdot \mathbf{k}_2) + \mu(\mathbf{k}_3 \cdot \mathbf{k}_2)(\mathbf{k}_4 \cdot \mathbf{k}_1)], \end{aligned} \quad (58)$$

$$\begin{aligned} & \left\langle \frac{\partial^4 V}{\partial h(\mathbf{k}_1) \partial h(\mathbf{k}_2) \partial u_{TA}(\mathbf{k}_3) \partial u_{TA}(\mathbf{k}_4)} \right\rangle_{\rho_V} \\ &= \frac{1}{\Omega} \delta_{\mathbf{k}_1+\mathbf{k}_2+\mathbf{k}_3+\mathbf{k}_4,0} \frac{\mathbf{k}_{3\perp} \cdot \mathbf{k}_{4\perp}}{|\mathbf{k}_3||\mathbf{k}_4|} [\lambda(\mathbf{k}_3 \cdot \mathbf{k}_4)(\mathbf{k}_1 \cdot \mathbf{k}_2) + \\ & \quad + \mu(\mathbf{k}_3 \cdot \mathbf{k}_1)(\mathbf{k}_4 \cdot \mathbf{k}_2) + \mu(\mathbf{k}_3 \cdot \mathbf{k}_2)(\mathbf{k}_4 \cdot \mathbf{k}_1)] \end{aligned} \quad (59)$$

and

$$\begin{aligned} & \left\langle \frac{\partial^4 V}{\partial h(\mathbf{k}_1) \partial h(\mathbf{k}_2) \partial u_{LA}(\mathbf{k}_3) \partial u_{TA}(\mathbf{k}_4)} \right\rangle_{\rho_V} = \\ & \frac{1}{\Omega} \delta_{\mathbf{k}_1+\mathbf{k}_2+\mathbf{k}_3+\mathbf{k}_4,0} \frac{\mathbf{k}_3 \cdot \mathbf{k}_{4\perp}}{|\mathbf{k}_3||\mathbf{k}_4|} [\lambda(\mathbf{k}_3 \cdot \mathbf{k}_4)(\mathbf{k}_1 \cdot \mathbf{k}_2) + \\ & \quad + \mu(\mathbf{k}_3 \cdot \mathbf{k}_1)(\mathbf{k}_4 \cdot \mathbf{k}_2) + \mu(\mathbf{k}_3 \cdot \mathbf{k}_2)(\mathbf{k}_4 \cdot \mathbf{k}_1)]. \end{aligned} \quad (60)$$

These equations cannot be further simplified, but we have all the ingredients to numerically calculate them. We have numerically checked that as in the atomistic case, the contribution of $\mathbf{D}^{(4)}$ is completely negligible. To show that we Taylor expand equation (11) as

$$\begin{aligned} \mathbf{\Pi}(z) &= \mathbf{M}^{-\frac{1}{2}} \mathbf{\Phi}^{(3)} \mathbf{\Lambda}(z) [\mathbf{I} - \mathbf{\Phi}^{(4)} \mathbf{\Lambda}(z)]^{-1} \mathbf{\Phi}^{(3)} \mathbf{M}^{-\frac{1}{2}} \simeq \\ & \simeq \mathbf{M}^{-\frac{1}{2}} \mathbf{\Phi}^{(3)} \mathbf{\Lambda}(z) \mathbf{\Phi}^{(3)} \mathbf{M}^{-\frac{1}{2}} + \mathbf{M}^{-\frac{1}{2}} \mathbf{\Phi}^{(3)} \mathbf{\Lambda}(z) \mathbf{\Phi}^{(4)} \mathbf{\Lambda}(z) \mathbf{\Phi}^{(3)} \mathbf{M}^{-\frac{1}{2}}, \end{aligned} \quad (61)$$

and we calculate the contribution of the term containing the fourth-order tensor to the linewidth. We also calculate the spectral function with and without the frequency dependence of self-energy. Extended Data Fig. 7 shows the results. This figure clearly shows that the contribution of the fourth-order tensor is at least one order of magnitude smaller than the main term, justifying the bubble approximation of the self-energy; more importantly, it also decays as momentum decreases. This figure also shows that the Lorentzian approximation is justified for the acoustic modes in graphene.

By neglecting the fourth-order terms containing the in-plane displacement fields in equation (36), which means that the potential is not rotationally invariant, the SCHA can be analytically applied in this model. The SCHA equations simplify to

$$\delta a = -\frac{1}{4\Omega} \sum_{\mathbf{q}} |\mathbf{q}|^2 g[\omega_{\text{SCHA}}^{(h)}(\mathbf{q})], \quad (62)$$

$$\begin{aligned} \Phi_{\text{SCHA}}^{(h)}(\mathbf{q}) &= \kappa |\mathbf{q}|^4 + 2\delta a (\lambda + \mu) |\mathbf{q}|^2 + \\ & + \frac{\lambda + 2\mu}{2\Omega} \sum_{\mathbf{k}} g[\omega_{\text{SCHA}}^{(\text{LA})}(\mathbf{k})] [|\mathbf{q}|^2 |\mathbf{k}|^2 + 2(\mathbf{q} \cdot \mathbf{k})^2]. \end{aligned} \quad (63)$$

By inserting equation (62) in equation (63) and considering the infinite-volume limit ($\Omega \rightarrow \infty$), we obtain

$$\Phi_{\text{SCHA}}^{(h)}(\mathbf{q}) = \kappa |\mathbf{q}|^4 + \gamma |\mathbf{q}|^2, \quad (64)$$

where γ is given by the solution

$$\gamma = \gamma \frac{\lambda + 3\mu}{16\pi\kappa\sqrt{\rho\kappa}} \int_0^{\Lambda\sqrt{\kappa/\gamma}} ds \frac{s^2 \coth[\gamma s \sqrt{1+s^2}/(2T\sqrt{\rho\kappa})]}{\sqrt{1+s^2}}. \quad (65)$$

Λ is an ultraviolet cutoff that avoids divergences. Equations (64) and (65) show that the dispersion of SCHA auxiliary ZA modes is linear.

By calculating the correction for getting the physical phonons in the static approach in equation (55) (in this case, the fourth-order tensor is 0), the result is

$$\Phi_F^{(h)}(\mathbf{q}) = \kappa |\mathbf{q}|^4 + (\gamma - \sigma) |\mathbf{q}|^2 + O(|\mathbf{q}|^4), \quad (66)$$

where at $T = 0$ K,

$$\sigma = \frac{\rho\sqrt{\gamma}}{8\pi\kappa^{3/2}} \sum_{\alpha=\text{LA,TA}} v_{\alpha} f(\Lambda\sqrt{\kappa/\gamma}, v_{\alpha}\sqrt{\rho/\gamma}), \quad (67)$$

with

$$f(x, y) = \int_0^x ds \frac{s^2}{\sqrt{1+s^2}[\sqrt{1+s^2}+y]}. \quad (68)$$

By setting the ultraviolet cutoff to the value of Debye momentum as $\Lambda = \sqrt{\frac{8\pi}{3\mu^2 a_0}} = 1.55 \text{ \AA}$, we obtain $1 - \sigma/\gamma = 20\%$. This means that the linear component of the physical frequencies turns out to be a factor 40% smaller than the one of the SCHA auxiliary frequency. The non-zero linear term in the physical frequencies appears because neglecting the fourth-order terms including in-plane displacements breaks the rotational invariance of the potential. This result suggests that the ultimate $q \rightarrow 0$ limit of the behaviour of physical phonons in the non-rotationally invariant case is linear at 0 K in this quantum theory.

Rotational invariance of membrane Hamiltonian

To explicitly prove that the membrane potential in equation (3) is rotationally invariant, let us consider a continuous elastic membrane embedded in three-dimensional space. Without a loss of generality, we assume that in the equilibrium configuration, the flat membrane lies in the x - y plane. We introduce the local deformations of the membrane from the flat geometry by means of the vector

$$\delta \mathbf{R}(\mathbf{r}) = u_x(\mathbf{r}) \mathbf{i} + u_y(\mathbf{r}) \mathbf{j} + h(\mathbf{r}) \mathbf{k}, \quad (69)$$

where $\mathbf{r} = x\mathbf{i} + y\mathbf{j}$ is the coordinate relative to the flat membrane, u_x and u_y are the in-plane displacements and h is the out-of-plane displacement. The strain tensor corresponding to the deformation in equation (69) is defined as

$$u_{ij} = \frac{1}{2} (\partial_i u_j + \partial_j u_i + \partial_i \mathbf{u} \cdot \partial_j \mathbf{u} + \partial_i h \partial_j h), \quad (70)$$

where we omitted the explicit dependence on \mathbf{r} for simplicity. The energy cost for the deformation is given by

$$\delta E = \frac{1}{2} \int d^2 r [C^{ijkl} u_{ij} u_{kl} + \kappa (\partial^2 h)^2], \quad (71)$$

where $ijkl = x, y$, $C^{ijkl} = \lambda \delta^{ij} \delta^{kl} + \mu (\delta^{ik} \delta^{jl} + \delta^{il} \delta^{jk})$ is the elastic moduli tensor, λ and μ are the Lamé coefficients and κ is the bending rigidity (as defined in the main text).

Hereafter, we show that the model of equation (71) is invariant under any rigid rotation about the plane of the membrane. To this purpose, we first define the rotation axis: $\mathbf{n} = n_x \mathbf{i} + n_y \mathbf{j}$, where $|\mathbf{n}| = 1$. The rigid rotation of the membrane about \mathbf{n} by angle θ is defined by the linear transformation

$$\mathbf{r} \rightarrow \mathbf{r}' = \exp[\theta \mathbf{n} \times] \mathbf{r}. \quad (72)$$

In this case, we can write

$$\delta \mathbf{R}(\mathbf{r}) = [\exp(\theta \mathbf{n} \times) - 1] \mathbf{r} = \sum_{k \geq 1} \frac{\theta^k}{k!} (\mathbf{n} \times)^k \mathbf{r}. \quad (73)$$

One can easily note that

$$\mathbf{n} \times \mathbf{r} = (n_x y - n_y x) \mathbf{k}, \quad (74a)$$

$$(\mathbf{n} \times)^2 \mathbf{r} = (n_x y - n_y x)(n_y \mathbf{i} - n_x \mathbf{j}), \quad (74b)$$

$$(\mathbf{n} \times)^{2k+1} \mathbf{r} = (-)^k \mathbf{n} \times \mathbf{r}, \quad (74c)$$

$$(\mathbf{n} \times)^{2k} \mathbf{r} = (-)^{k-1} (\mathbf{n} \times)^2 \mathbf{r}, \quad (74d)$$

and then write equation (73) as

$$\delta \mathbf{R}(\mathbf{r}) = \sin \theta (\mathbf{n} \times \mathbf{r}) + (1 - \cos \theta) [(\mathbf{n} \times)^2 \mathbf{r}]. \quad (75)$$

Identifying equations (69) and (75) and using equation (74) yields

$$u_x(\mathbf{r}) = u_x^0 f(\mathbf{r}), \quad u_y(\mathbf{r}) = u_y^0 f(\mathbf{r}), \quad h(\mathbf{r}) = h^0 f(\mathbf{r}), \quad (76a)$$

where

$$(u_x^0, u_y^0, h^0) = [n_y(1 - \cos \theta), -n_x(1 - \cos \theta), \sin \theta] \quad (76b)$$

and

$$f(\mathbf{r}) = n_x y - n_y x. \quad (76c)$$

The strain tensor in equation (70) can then be written as

$$u_{ij} = \frac{1}{2} \left\{ u_i^0 \partial_j f + u_j^0 \partial_i f + \left[(u_x^0)^2 + (u_y^0)^2 + (h^0)^2 \right] \partial_i f \partial_j f \right\}. \quad (77)$$

It is straightforward to show that equation (76) implies $u_{ij} = 0 \forall ij$. Concerning the term $\kappa(\partial^2 h)^2$ in equation (71), it is trivially zero as h is a linear function of \mathbf{r} in the rigid rotation that we are considering. This finally shows that $\delta E = 0$ for any rigid rotation about the membrane's plane. Note that the $\partial_i \mathbf{u} \cdot \partial_j \mathbf{u}$ term in the potential is needed to keep $\delta E = 0$. When it is neglected, $\delta E \neq 0$ for a rigid rotation.

Equal-time height–height correlation function within SCHA

Within an interacting picture, the ensemble average of any displacement–displacement correlation function is given by the following equal-time Green's function (we use $\hbar = k_B = 1$):

$$\sqrt{M_a M_b} \langle u_a u_b \rangle = G^{ab}(\tau = 0^+) = -T \sum_n G^{ab}(i\Omega_n), \quad (78)$$

where $G^{ab}(i\Omega_n)$ is the SCHA Green's function in the frequency domain for the variable $\sqrt{M_a}(R^a - \mathcal{R}_{eq}^a)$ defined in equation (2) and $\Omega_n = 2\pi T n$ are the bosonic Matsubara's frequencies. \mathcal{R}_{eq}^a are the centroid positions that minimize the SCHA free energy.

The summation has to be done via the Lehmann representation:

$$\sqrt{M_a M_b} \langle u_a u_b \rangle = -T \sum_n G^{ab}(i\Omega_n) = \int_{-\infty}^{\infty} \frac{d\omega}{2\pi} \tilde{\sigma}(\omega) n_B(\omega), \quad (79)$$

where $\tilde{\sigma}(\omega)$ is the spectral function of Green's function, defined in this case as: $\tilde{\sigma}(\omega) = -2\text{Im}[G(\omega + i0^+)]$. Retaining only the first term of the dynamical SCHA self-energy (bubble approximation) and neglecting mode mixing, the spectral function resembles a superposition of Lorentzians, but with frequency-dependent shifts and widths. When the quasiparticle picture is valid after the inclusion of anharmonicity, the spectral function can actually be expressed as a superposition of Lorentzians:

$$\tilde{\sigma}(\omega) = \sum_{\mu} \epsilon_{\mu}^a \epsilon_{\mu}^b \left(\frac{1}{\omega} \left[\frac{\Gamma_{\mu}}{(\omega - \Theta_{\mu})^2 + (\Gamma_{\mu})^2} + \frac{\Gamma_{\mu}}{(\omega + \Theta_{\mu})^2 + (\Gamma_{\mu})^2} \right] \right), \quad (80)$$

where Θ_{μ} is the frequency of SCHA quasiparticle in the Lorentzian approximation and Γ_{μ} is the half-width at half-maximum.

We can avoid divergences in the integral by redefining the sum as

$$\sqrt{M_a M_b} \langle u_a u_b \rangle = -T G^{ab}(0) + \int_{-\infty}^{\infty} \frac{d\omega}{2\pi} \tilde{\sigma}(\omega) \left[n_B(\omega) - \frac{T}{\omega} \right]. \quad (81)$$

Regarding the first term in the sum, the static limit of Green's function corresponds to the inverse of the free energy dynamical matrix:

$$G^{ab}(i\Omega_n = 0) = -[D^{(F)}]_{ab}^{-1} = \sum_{\mu} \epsilon_{\mu}^a \epsilon_{\mu}^b \left(-\frac{1}{\Omega_{\mu}^2} \right), \quad (82)$$

where Ω_{μ} are the frequencies of free energy phonons.

Inserting equations (82) and (80) in equation (81), we get

$$\begin{aligned} \sqrt{M_a M_b} \langle u_a u_b \rangle &= \sum_{\mu} \epsilon_{\mu}^a \epsilon_{\mu}^b \left(\frac{T}{\Omega_{\mu}^2} + \int_{-\infty}^{\infty} \frac{d\omega}{2\pi} \times \right. \\ &\times \left. \left(\frac{1}{\omega} \left[\frac{\Gamma_{\mu}}{(\omega - \Theta_{\mu})^2 + (\Gamma_{\mu})^2} + \frac{\Gamma_{\mu}}{(\omega + \Theta_{\mu})^2 + (\Gamma_{\mu})^2} \right] \right) \times \right. \\ &\times \left. \left[n_B(\omega) - \frac{T}{\omega} \right] \right). \end{aligned} \quad (83)$$

This integral can be simplified when the phonon–phonon linewidth tends to zero. For those cases, the Lorentzian representation of the Dirac delta function can be used:

$$\delta(x) = \frac{1}{\pi} \lim_{\epsilon \rightarrow 0^+} \frac{\epsilon}{x^2 + \epsilon^2}. \quad (84)$$

Then,

$$\begin{aligned} \sqrt{M_a M_b} \langle u_a u_b \rangle &= \sum_{\mu} \epsilon_{\mu}^a \epsilon_{\mu}^b \left(\frac{T}{\Omega_{\mu}^2} + \frac{1}{2} \int_{-\infty}^{\infty} d\omega \times \right. \\ &\times \left. \left(\frac{1}{\omega} \times [\delta(\omega - \Theta_{\mu}) + \delta(\omega + \Theta_{\mu})] \right) \left[n_B(\omega) - \frac{T}{\omega} \right] \right) \end{aligned} \quad (85)$$

and

$$\langle u_a u_b \rangle = \frac{\sum_{\mu} \epsilon_{\mu}^a \epsilon_{\mu}^b}{\sqrt{M_a M_b}} \left(\frac{T}{\Omega_{\mu}^2} + \frac{-n_B(-\Theta_{\mu}) + n_B(\Theta_{\mu})}{2\Theta_{\mu}} - \frac{T}{\Theta_{\mu}^2} \right).$$

Finally, when free energy Hessian phonons (physical phonons in the static approach) and physical ones are nearly identical ($\Omega_{\mu}^2 \approx \Theta_{\mu}^2$), we recover the formula of the non-interacting case but evaluated with free energy Hessian (equivalently, physical) phonons:

$$\begin{aligned} \langle u_a u_b \rangle &= \frac{\sum_{\mu} \epsilon_{\mu}^a \epsilon_{\mu}^b}{\sqrt{M_a M_b}} \left[\frac{(n_B[\Omega_{\mu}] - n_B[-\Omega_{\mu}])}{2\Omega_{\mu}} \right] = \\ &= \frac{\sum_{\mu} \epsilon_{\mu}^a \epsilon_{\mu}^b}{\sqrt{M_a M_b}} \left[\frac{(1 + 2n_B[\Omega_{\mu}])}{2\Omega_{\mu}} \right]. \end{aligned} \quad (86)$$

In the case of the membrane model, the displacement–displacement correlation function is given by

$$\langle u_a(\mathbf{x})u_b(\mathbf{x}') \rangle = \frac{\sum_{\mu} \epsilon_{\mu}^a(\mathbf{x})\epsilon_{\mu}^b(\mathbf{x}')}{\rho} \left[\frac{(1 + 2n_B[\Omega_{\mu}])}{2\Omega_{\mu}} \right], \quad (87)$$

where a and b are the Cartesian indexes and $\mu = h$, LA and TA in this case. Essentially, discrete magnitudes are now continuous, whereas the individual atomic masses M_a and M_b are replaced by the mass density of the membrane ρ . The corresponding Fourier transform is given by

$$\langle u_a(\mathbf{q})u_b(\mathbf{k}) \rangle = \delta_{\mathbf{q},-\mathbf{k}} \frac{\sum_{\mu} \epsilon_{\mu}^a(\mathbf{q})\epsilon_{\mu}^b(-\mathbf{q})}{\rho} \left[\frac{(1 + 2n_B[\Omega_{\mu}(\mathbf{q})])}{2\Omega_{\mu}(\mathbf{q})} \right]. \quad (88)$$

We are particularly interested in the Fourier transform of the out-of-plane correlation function. As in the membrane model, ZA is the only mode with an out-of-plane component; we finally obtain

$$\langle |h(\mathbf{q})|^2 \rangle = \frac{(1 + 2n_B[\Omega_{ZA}(\mathbf{q})])}{2\rho\Omega_{ZA}(\mathbf{q})}, \quad (89)$$

which is the formula implemented to obtain the Fourier transform of the height–height correlation function.

Nearly all the approximations taken in this mathematical derivation have been demonstrated for graphene throughout here. The only task left is showing that the linewidth of the ZA mode is as small as the ones corresponding to the in-plane phonon modes, which is indeed true (Extended Data Fig. 8).

Extra calculations of the equal-time height–height correlation function

The out-of-plane correlation function is governed by the bosonic occupation factor. Quantum correlations appear for those flexural modes that are barely occupied thermally, that is, in those modes whose quantum zero-point energy is bigger than the thermal energy:

$$\frac{1}{2}\hbar\omega_{ZA}(\mathbf{q}) > k_B T \Leftrightarrow q_T > \left(\sqrt{\frac{\rho}{\kappa}} \frac{2k_B T}{\hbar} \right). \quad (90)$$

Decreasing the temperature and/or increasing the wavelength favours the emergence of quantum correlations⁵¹.

In this subsection, we provide extra calculations analysing the extreme cases at 0 and 300 K. At null temperature, there is no thermally occupied phonon mode, but all of them fluctuate due to quantum zero-point motion. Then, the height–height correlation function shows a fully quantum behaviour, with no crossover to a classical regime (Extended Data Fig. 9). The harmonic and anharmonic rotational invariant results yield the same exponents due to quadratic dispersion: $\langle |h(\mathbf{q})|^2 \rangle \propto q^{-2}$. The anharmonic non-rotational invariant phonons are quadratic in the short-wavelength limit, but they are linearized in the long-wavelength limit, with $\langle |h(\mathbf{q})|^2 \rangle \propto \Omega_{ZA}(\mathbf{q})^{-1} \propto q^{-1.62}$. This exponent coincides with the one obtained in the SCSA, which scales as q^{ν} , where $\nu \approx 1.6$ (ref. 49).

At 300 K, the classical-to-quantum crossover occurs at 1.18 \AA^{-1} ; therefore, all the modes are largely occupied in the q range in which we have focused our analysis. Thermal fluctuations rule and the height–height correlation function shows a classical behaviour (Extended Data Fig. 10). Again, the quadratic dispersion of the harmonic and anharmonic rotational invariant results is behind the exponent of the correlation function, which is now $\langle |h(\mathbf{q})|^2 \rangle \propto q^{-4}$, as predicted by classical statistics. The linearization of anharmonic phonons in the long-wavelength limit when the rotational invariance is broken makes us recover the exponent obtained in the classical counterparts in the literature.

Dependence of ZA frequency on strain

To assess the relevance of small strains on the behaviour of the height–height correlation function, we formulate a simple harmonic model

that describes the relationship between the ZA frequency and the biaxial strain δa . In equation (40), the only second-order term involving h is $\delta a(\lambda + \mu) \int_{\Omega} d^2x \partial_x h \partial_x h$. Consequently, the modified harmonic potential energy for h due to strain can be expressed as

$$U_{\delta a} = \frac{1}{2} \left[\int_{\Omega} d^2x \kappa (\partial^2 h)^2 + 2\delta a(\lambda + \mu) \int_{\Omega} d^2x \partial_x h \partial_x h \right], \quad (91)$$

whose diagonalization leads to

$$\omega_{ZA}(q) = \sqrt{\frac{2(\lambda + \mu)\delta a q^2 + \kappa q^4}{\rho}}. \quad (92)$$

We plug equation (92) in the equation for the height–height correlation function in the main text (equation (5)) and explicitly calculate $\langle |h(\mathbf{q})|^2 \rangle$ at $T = 12.5 \text{ K}$. Extended Data Fig. 2 shows the obtained result. A strain as small as $\delta a = 10^{-5}$ can deviate the ripple amplitude from the q^{-4} law, lowering it to $q^{-3.23}$.

Data availability

Source data are provided with this paper. All other data are available from the corresponding author upon reasonable request.

Code availability

The atomistic calculations of the SCHA theory are performed with the SSCHA code. This code is open source and can be downloaded from <https://sscha.eu/>. The SCHA calculations in the membrane model are performed with an in-house program adapting the distributed SCHA code, which is available from the corresponding author upon reasonable request.

References

54. Mahan, G. *Many-Particle Physics*. (Springer, 2000).
55. Dion, M., Rydberg, H., Schröder, E., Langreth, D. C. & Lundqvist, B. I. Van der Waals density functional for general geometries. *Phys. Rev. Lett.* **92**, 246401 (2004).
56. Perdew, J. P., Burke, K. & Ernzerhof, M. Generalized gradient approximation made simple. *Phys. Rev. Lett.* **77**, 3865 (1996).
57. Vanderbilt, D. Soft self-consistent pseudopotentials in a generalized eigenvalue formalism. *Phys. Rev. B* **41**, 7892 (1990).
58. Barone, V. et al. Role and effective treatment of dispersive forces in materials: polyethylene and graphite crystals as test cases. *J. Comput. Chem.* **30**, 934–939 (2009).
59. Monkhorst, H. J. & Pack, J. D. Special points for Brillouin-zone integrations. *Phys. Rev. B* **13**, 5188 (1976).
60. Ypma, T. J. Historical development of the Newton–Raphson method. *SIAM Rev.* **37**, 531–551 (1995).

Acknowledgements

We would like to thank F. Guinea for useful conversations. Financial support was provided by the Spanish Ministry of Economy and Competitiveness (FIS2016-76617-P); the Spanish Ministry of Science and Innovation (grant nos. PID2019-105488GB-I00 and PID2022-142861NA-I00); the Department of Education, Universities and Research of the Basque Government and the University of the Basque Country (IT1707-22 and IT1527-22); and the European Commission under the Graphene Flagship, Core3, grant no. 881603. M.C. acknowledges support from ICSC—Centro Nazionale di Ricerca in HPC, Big Data and Quantum Computing, funded by the European Union under NextGenerationEU. U.A. is thankful to the Material Physics Center for a predoctoral fellowship. J.D. thanks the Department of Education of the Basque Government for a predoctoral fellowship (grant no. PRE-2020-1-0220). L.M. acknowledges funding support from the European Union under the Marie Curie Individual Fellowship

THERMOH. Computer facilities were provided by the Donostia International Physics Center (DIPC).

Author contributions

U.A. and J.D. contributed equally. U.A. performed the atomistic calculations, whereas U.A., J.D. and T.C. performed the calculations on the membrane and developed the theoretical adaptation of SCHA theory to the membrane. L.M., T.C., R.B. and I.E. developed the mathematical proof of the relation between Green's function and free energy Hessian. I.E. and F.M. supervised the full project. The manuscript was written by U.A., J.D. and I.E., with input from all authors.

Competing interests

The authors declare no competing interests.

Additional information

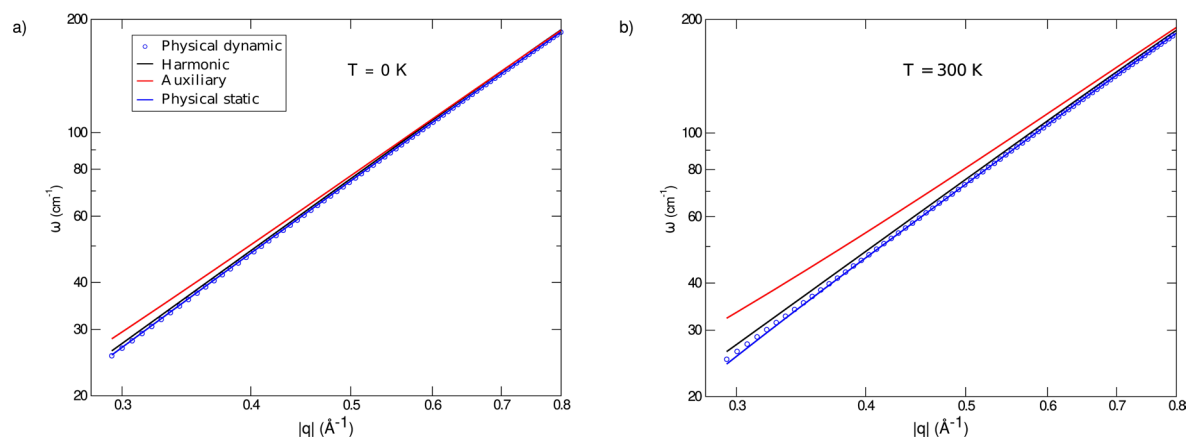
Extended data is available for this paper at <https://doi.org/10.1038/s41567-024-02441-z>.

Supplementary information The online version contains supplementary material available at <https://doi.org/10.1038/s41567-024-02441-z>.

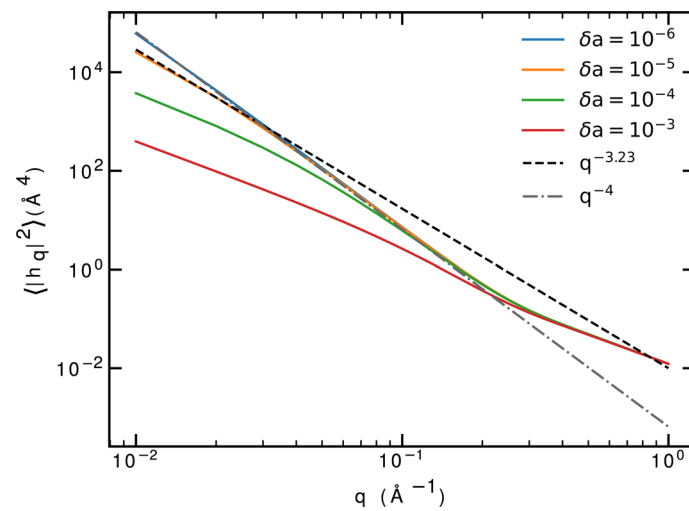
Correspondence and requests for materials should be addressed to Ion Errea.

Peer review information *Nature Physics* thanks the anonymous reviewers for their contribution to the peer review of this work.

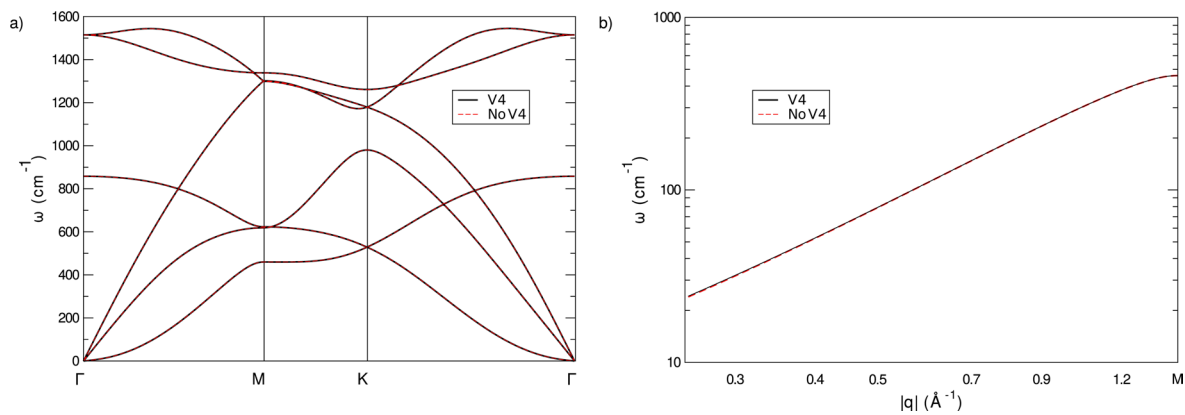
Reprints and permissions information is available at www.nature.com/reprints.



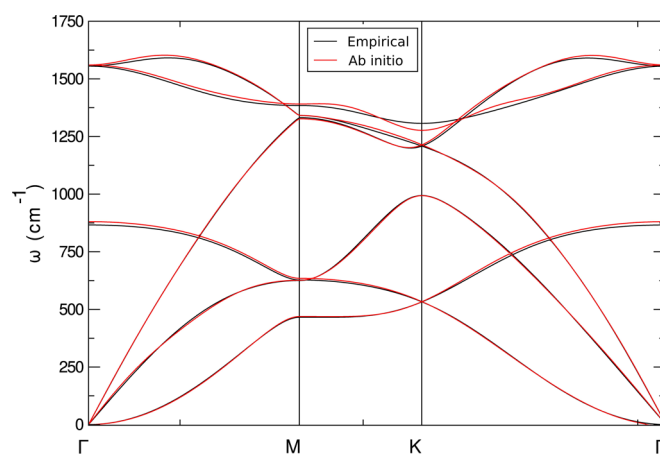
Extended Data Fig. 1 | Negligible dynamic effects in the ZA mode frequencies. Harmonic, and SCHA auxiliary and physical phonons (static and dynamic) calculated at 0 K (a) and 300 K (b) with the atomistic potential for the ZA mode.



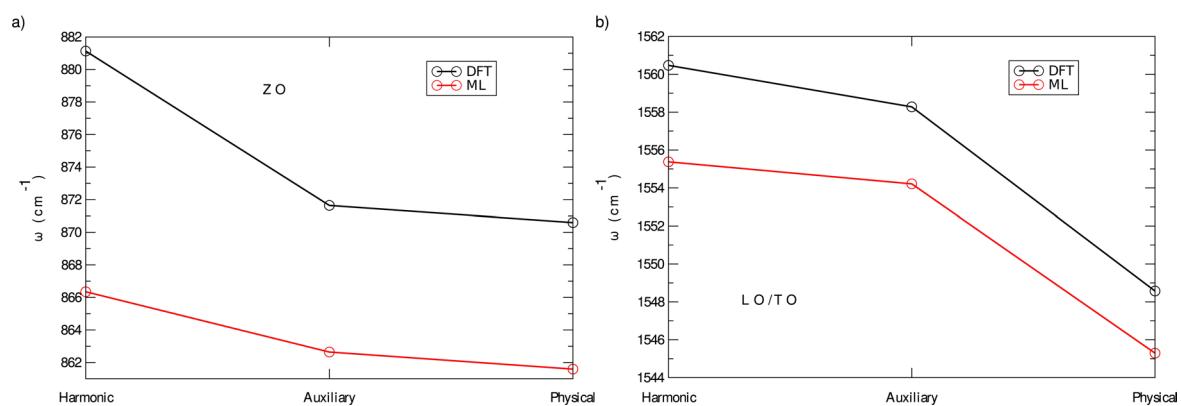
Extended Data Fig. 2 | Height-height correlation function as a function of the biaxial strain δa . Impressively, the behavior for small q deviates from the q^{-4} law even for very small strains, for example $\delta a = 10^{-5}$.



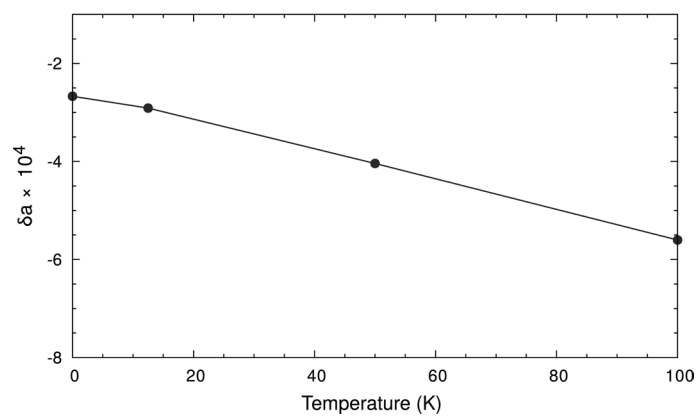
Extended Data Fig. 3 | Bubble approximation in the static limit of the SCHA theory. (a) Physical phonons in the static approach with the atomistic potential at 500 K including and neglecting $\Phi^{(4)}$ in Eq. (11). (b) panel only includes the ZA modes and it is in logarithmic scale. The calculation is done in a 6×6 supercell.



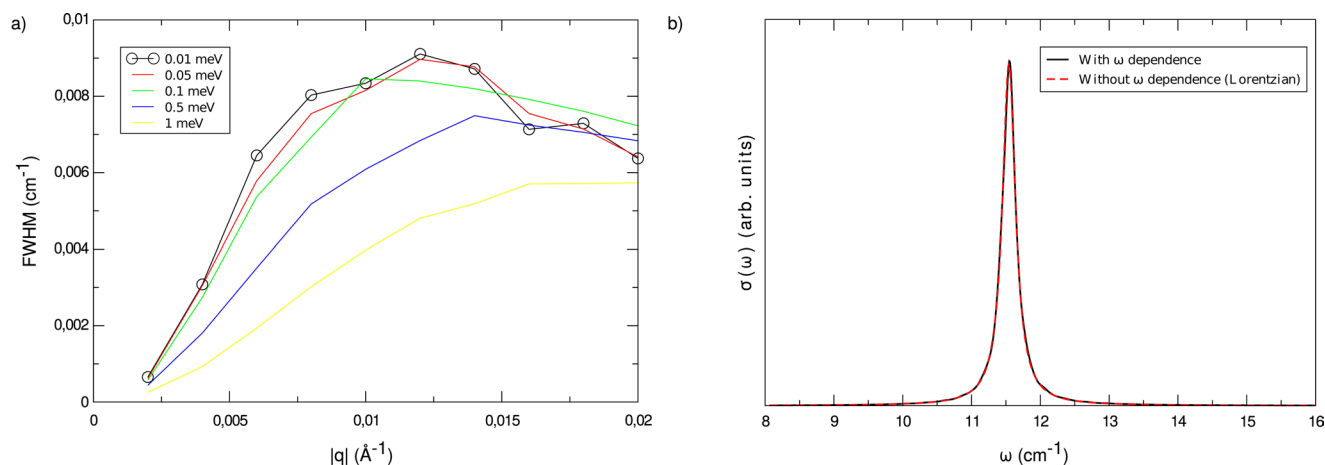
Extended Data Fig. 4 | Empirical potential benchmark I. Harmonic phonon spectrum of graphene calculated with the machine learning empirical potential and ab initio. The calculations are done in a 6×6 supercell.



Extended Data Fig. 5 | Empirical potential benchmark II. Harmonic, and SCHA auxiliary and physical frequencies (static) using the DFT and machine learning (ML) forces. (a) panel shows the out-of-plane optical frequency at the Γ point and (b) panel the in-plane one.

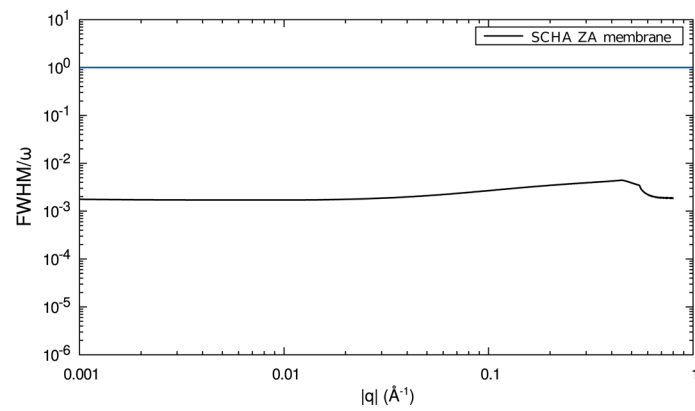


Extended Data Fig. 6 | Negative thermal expansion of graphene in the membrane model. δa as a function of temperature in the membrane model.

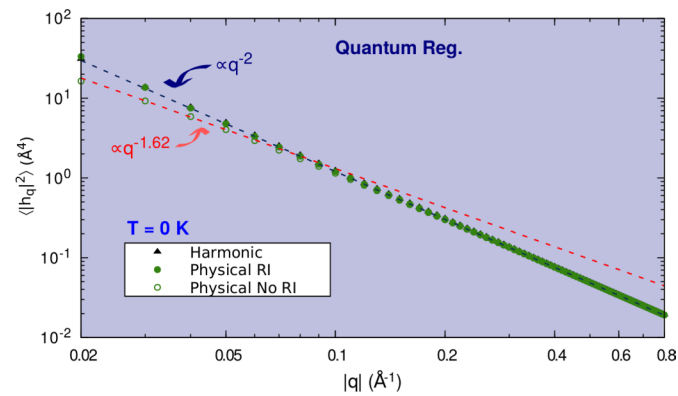


Extended Data Fig. 7 | Justification of the bubble and Lorentzian approximations in the calculation of spectral properties of the LA mode within the membrane model. (a) Linewidth (full width at half maximum, FWHM) contribution of the term containing the fourth-order tensor of the LA

mode calculated in the membrane model at 100 K using the harmonic and SCHA auxiliary phonons. The value of the smearing is in the legend. (b) Spectral function of the LA mode with momentum 0.01 \AA^{-1} with and without considering the frequency dependence of the self energy.

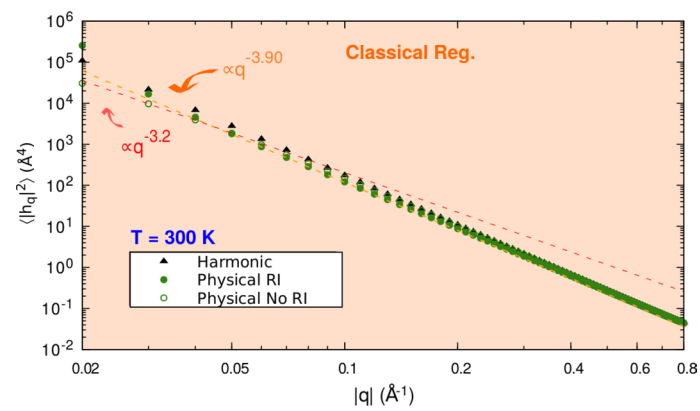


Extended Data Fig. 8 | Anharmonicity does not remove the quasiparticle picture of ZA modes. Linewidth (full width half maximum) of ZA phonon mode divided by its frequency at 300K calculated within the membrane model. The ratio never gets bigger than 1.



Extended Data Fig. 9 | Height-height correlation function showing a pure quantum behaviour. Fourier transform of the height-height correlation function at 0 K in the membrane model evaluated at different levels of approximation: harmonic (black dots), anharmonic rotationally invariant (RI)

result (green filled dots) and anharmonic no rotationally invariant (No RI) result (green empty dots). The dashed lines correspond to the linear fitting in each case.



Extended Data Fig. 10 | Height-height correlation function showing a pure classical behaviour. Fourier transform of the height-height correlation function at 300 K in the membrane model evaluated at different levels of approximation:

harmonic (black dots), anharmonic RI result (green filled dots) and anharmonic No RI result (green empty dots). The dashed lines correspond to the linear fitting in each case.